Supplemental material to this article can be found at:
http://jpet.aspetjournals.org/content/suppl/2018/03/19/jpet.117.247163.DC1

1521-0103/365/2/354–367$35.00
THE JOURNAL OF PHARMACOLOGY AND EXPERIMENTAL THERAPEUTICS
Copyright © 2018 by The Author(s)
This is an open access article distributed under the CC BY-NC Attribution 4.0 International license.
https://doi.org/10.1124/jpet.117.247163
J Pharmacol Exp Ther 365:354–367, May 2018

The Journal of PHARMACOLOGY And Experimental Therapeutics

Identification and Characterization of Novel Receptor-Interacting Serine/Threonine-Protein Kinase 2 Inhibitors Using Structural Similarity Analysis[S]

Mohamed Salla, Rodrigo Aguayo-Ortiz, Gaddafi I. Danmaliki, Alaa Zare, Ahmed Said, Jack Moore, Vrajeshkumar Pandya, Robin Manaloor, Sunny Fong, Anna R. Blankstein, Spencer B. Gibson, Laura Ramos Garcia, Pascal Meier, Khushwant S. Bhullar, Basil P. Hubbard, Yahya Fiteh, Harissios Vliagoftis, Ing Swie Goping, Dion Brocks, Peter Hwang, Carlos A. Velázquez-Martínez, and Shairaz Baksh

Departments of Biochemistry (M.S., G.I.D., A.S., J.M., V.P., I.S.G., P.H., S.B.), Pediatrics (A.Z., R.M., S.F., S.B.), Pharmacology (K.S.B., B.P.H.), Oncology (S.B.) Medicine (Y.F., H.V., P.H.), and Faculty of Pharmacy and Pharmaceutical Sciences (R.A.-O., D.B., C.A.-V.M.), University of Alberta, Edmonton, Alberta, Canada; Facultad de Química, Departamento de Farmacia, Universidad Nacional Autónoma de México, Mexico City, Mexico (R.A.-O.); Departments of Biochemistry and Medical Genetics and Immunology, University of Manitoba, Winnipeg, Manitoba, Canada (A.R.B., S.B.G.); Breakthrough Breast Cancer Research Center Chester Beatty Laboratories, London, United Kingdom (L.R.G., P.M.); Cancer Research Institute of Northern Alberta, Edmonton, Alberta, Canada (S.B.); and Women and Children's Health Research Institute, Edmonton, Alberta, Canada (S.B.)

Received December 13, 2017; accepted February 26, 2018

ABSTRACT

Receptor-interacting protein kinase 2 (RIP2 or RICK, herein referred to as RIPK2) is linked to the pathogen pathway that activates nuclear factor κ-light-chain-enhancer of activated B cells (NFκB) and autophagic activation. Using molecular modeling (docking) and chemoinformatics analyses, we used the RIPK2/ponatinib crystal structure and searched in chemical databases for small molecules exerting binding interactions similar to those exerted by ponatinib. The identified RIPK2 inhibitors potently inhibited the proliferation of cancer cells by > 70% and also inhibited NFκB activity. More importantly, in vivo inhibition of intestinal and lung inflammation rodent models suggests effectiveness to resolve inflammation with low toxicity to the animals. Thus, our identified RIPK2 inhibitor may offer possible therapeutic control of inflammation in diseases such as inflammatory bowel disease, asthma, cystic fibrosis, primary sclerosing cholangitis, and pancreatitis.

Introduction

Activation of nuclear factor κ-light-chain-enhancer of activated B cells (NFκB) proceeds through multiple pathways involving tumor necrosis factor receptor 1 (TNF-R1) and pathogen-recognition receptors, such as Toll-like receptors (TLRs) (Orlowski and Baldwin, 2002; Madrid and Baldwin, 2003; Hayden and Ghosh, 2004) and nucleotide-binding oligomerization domain-containing protein 2 (NOD2), an intracellular pattern-recognition receptor. NOD2 is mainly stimulated by muramyl dipeptide (MDP), a bacterial product found in both Gram-positive and Gram-negative bacteria, and requires the obligate kinase, receptor-interacting protein kinase 2 (RIPK2), to promote both NFκB activation and an autophagic response (Tigno-Aranjuez et al., 2010). Mice with genetic deletion of *Nod2*/*Ripk2* have a dysbiotic intestinal flora, resulting in altered susceptibility to intestinal

The research in this study was supported by grants from Alberta Innovates – Health Solutions CRIO, Alberta Heritage Foundation for Medical Research, from the division of Hematology/Oncology/Palliative Care/ Epidemiology under Dr. David Eisenstat for funds to partially support this project and from the Department of Pediatrics/Stollery Children's Hospital-WCHRI Hair Massacure Donation Fund. Aguayo-Ortiz is very grateful to CONACyT (Mexico) for the fellowship granted (No. 510728/288862).

Authors M. Salla and R.Aguayo-Ortiz contributed equally to this manuscript.

https://doi.org/10.1124/jpet.117.247163.

[S] This article has supplemental material available at jpet.aspetjournals.org.

ABBREVIATIONS: 5-ROESY, rotating-frame overhauser enhancement spectroscopy; BAL, bronchoalveolar lavage; CRC, colorectal cancer; DMSO, dimethylsulfoxide; DSS, dextran sulfate sodium; IBD, inflammatory bowel disease; IL, interleukin; IP, immunoprecipitation; LPS, lipopolysaccharide; MDP, muramyl dipeptide; MolPort-016-359-762, 3-benzamido-4-methyl-*N*-[3-(1-methyl-1H-imidazol-2yl)phenyl]benzamide; MTT, (3-(4,5-dimethylthiazol-2-Yl)-2,5-diphenyltetrazolium bromide); NFκB, nuclear factor κ-light-chain-enhancer of activated B cells; NOD2, nucleotide-binding oligomerization domain-containing protein 2; OD36, 6-Chloro-10,11,14,17-tetrahydro-13H-1,16-etheno-4,8-metheno-1H-pyrazolo[3,4-g][1,14,4,6]dioxadiazacyclohexadecine; OD38, 4,5,8,9-Tetrahydro-7H-2,17-etheno-10,14-metheno-1H-imidazo[1,5-g][1,4,6,7,12,14] oxapentaazacyclohexadecine; PDB, Protein Data Bank; RASSF1A, Ras association domain family protein 1A; RIPK2, receptor-interacting protein kinase 2; ROE, rotating-frame nuclear Overhauser enhancement; SIRT1, sirtuin 1; TLR, Toll-like receptor; TNF, tumor necrosis factor; WEHI-435, N-(2-(4-amino-3-(p-tolyl)-1H-pyrazolo[3,4-d]pyrimidin-1-yl)-2-methylpropyl)isonicotinamide.

Downloaded from jpet.aspetjournals.org at ASPET Journals on April 4, 2018

inflammation (Ermann et al., 2014). In addition, the loss of *Ripk2* has been demonstrated to result in the inability of cells to carry out mitophagy, leading to enhanced mitochondrial production of superoxide/reactive oxygen species and accumulation of damaged mitochondria that will trigger a caspase 1–dependent inflammasome activation (Lupfer et al., 2014). In the context of malignant transformation, knockdown of RIPK2 downregulated mRNA expression of E-cadherin and vimentin, both of which are involved in epithelial to mesenchymal transition and metastatic promotion (Wu et al., 2012). RIPK2 might thus play an important role in cell migration (Wu et al., 2012), metastasis (Wu et al., 2012), and offer alternate novel therapeutics for abnormal inflammation driven by the NOD2/RIPK2 pathway.

Most RIPK2 inhibitors were not designed to inhibit RIPK2, and thus, RIPK2 inhibition was an off-target effect of the use of these drugs. These included gefitinib/Iressa (IC_{50} at 50 nM) (Canning et al., 2015), regorafenib, and other protein tyrosine kinases (Canning et al., 2015). Tigno-Aranjuez et al. (2014) reported on the identification of a novel class of RIPK2 inhibitors (OD36 [6-Chloro-10,11,14,17-tetrahydro-13H-1,16-etheno-4,8-metheno-1H-pyrazolo[3,4-g][1,14,4,6]dioxadiazacyclohexadecine] and OD38 [4,5,8,9-Tetrahydro-7H-2,17-etheno-10,14-metheno-1H-imidazo[1,5-g][1,4,6,7,12,14]oxapentaazacyclohexadecine]) that can inhibit 92% kinase activity of RIPK2 at 100 nM and can alleviate inflammation in a rodent model for inflammatory bowel disease. However, like most RIPK2 inhibitors, at 100 nM, >80% inhibition of 10-FYN proto-ocogene, transforming growth factor 2 beta, activin receptor like kinase 2, and lymphocyte specific protein tyrosine kinase and Lck was also observed. WEHI-435, a recently characterized small-molecule RIPK2 inhibitor, was demonstrated to delay RIPK2 ubiquitination and NFκB activation downstream of NOD2 activation. In addition, WEHI-435 (N-(2-(4-amino-3-(p-tolyl)-1H-pyrazolo [3,4-d]pyrimidin-1-yl)-2-methylpropyl)isonicotinamide) interfered with cytokine production in vitro and in vivo and ameliorated experimental autoimmune encephalomyelitis in mice (Nachbur et al., 2015). Recently, GlaxoSmithKline isolated an RIPK2 inhibitor, GSK-583 (6-(tert-butylsulfonyl)-N-(5-fluoro-1H-indazol-3-yl)quinolin-4-amine), based on using the full RIPK2 protein to screen a DNA-encoded library collection with a fluorescence polarization–based binding assay as a readout (Haile et al., 2016). This bound to the ATP binding pocket of the kinase domain and inhibited RIPK2 with an IC_{50} of 5–50 nM, depending on the assay. Last, Novartis recently reported on their RIPK2 inhibitor, obtained by virtual screening of their proprietary library, that can inhibit RIPK2 with an IC_{50} of 3 nM (He et al., 2017). No in vivo applicability was analyzed, but it can selectively inhibit MDP-promoted cytokine production in peripheral blood mononuclear cells and bone marrow–derived mouse macrophages. A kinome analysis was not carried out, and thus, it is unknown if significant off-target effects exist in the presence of the Novartis RIPK2 inhibitor.

Because of robust off-target effects of most RIPK2 inhibitors, we carried out molecular modeling (docking) and cheminformatics analyses by carefully analyzing the only known crystal structure of RIPK2 in association with the c-ABL kinase inhibitor ponatinib (https://www.rcsb.org/pdb/explore/macroMoleculeData.do?structureId=4C8B). Utilizing this structure, we searched chemical databases for scaffolds exerting significant binding interactions similar to (or stronger than) those exerted by ponatinib, determined by comparing their free energies when docked inside of the RIPK2 binding site. In addition to RIPK2 binding as part of this computer-based (initial) screening, we selected compounds that inhibited epidermal growth factor receptor (IC_{50} values >1000 nM; weak inhibitory activity) along with weak binding interactions in the EGFR and c-ABL binding sites, two common off-targets for previously identified RIPK2 inhibitors. Several hits are shown in Fig. 1 and Table 1, and these compounds have unknown biologic features. Since RIPK2 signals downstream of NOD2 and is linked to NFκB and autophagy activation, we speculated that the in vivo use of our selective RIPK2 inhibitors would target NFκB activation and possibly resolve abnormal inflammation states.

Methods

Additional methods can be found in the Supplemental Experimental Procedures online.

Pharmacophore Search. Commercially available subsets of the ZINC (15,868,179 compounds) and MolPort (7,241,662 compounds) databases were screened using the lead drug ponatinib as a reference. We used the ZINCPharmer pharmacophore search server (Koes and Camacho, 2012), and pharmacophore features were identified directly from the RIPK2 structure [Protein Data Bank (PDB) identifier: 4C8B] and used for the screening. In this regard, a total of 74 compounds were selected from both databases. The selected compounds were then docked into the RIPK2 binding site.

Structure Similarity Search. The PubChem (Kim et al., 2016) compound library (more than 80 million molecules) was compared with ponatinib to filter all molecules which are at least 60% similar to this compound (10,655,787 molecules). We selected the most similar (≥90%; 803 compounds) and less similar (<62%; 50,000 compounds randomly selected from a total of 2,607,266) structures using the PubChem Fingerprint implemented in the ChemmineR package (Bioconductor, Seattle, WA) (Cao et al., 2008) of the R program (R Development Group, Vienna, Austria). The filtered compounds were then subjected to another filtering step based on Lipinski's rule of five (Lipinski et al., 2001), removing the duplicates and inorganic molecules with the FAFDrugs3 server (Lagorce et al., 2015) (22,274 compounds). Finally, a total of 3000 compounds were selected and optimized using the *obminimize tool* of the OpenBabel toolbox (Open Babel, Pittsburgh, PA) (O'Boyle et al., 2011) for the docking studies.

Molecular Docking. The crystal structure of the human RIPK2 (PDB: 4C8B) (https://www.rcsb.org/pdb/explore/macroMoleculeData.do?structureId=4C8B) was retrieved from the PDB (Bernstein et al., 1977). Some residues in the three-dimensional structures were missing, and consequently, these side-chain atoms were added using the WHAT IF web interface (Vriend, 1990). The protein was subjected to an energy minimization using the AMBER99SB force field by 1000-step steepest-descent minimization followed by 100-conjugate gradient minimization using University of California, San Francisco CHIMERA version 1.9 software (University of California, San Francisco, CA) (Pettersen et al., 2004). Polar hydrogens, Gasteiger-Marsili empirical atomic partial charges, and the AutoDock atom types were computed using the MGLTools version 1.5.4 package (Molecular Graphics Laboratory at The Scripps Research Institute, La Jolla, CA) (Morris et al., 2009). The torsional root and branches of the ligands were chosen with the same program, allowing flexibility for all rotational bonds (except for the amide bond). In addition, the software was used to assign Gasteiger-Marsili atomic charges to all ligands (Gasteiger et al., 1978). Docking calculations were performed using the AutoDock Vina software (Molecular Graphics Lab at The Scripps Research Institute) (Trott and Olson, 2010). A grid box of 28 $Å^3$ and centered at the binding site was used to calculate the atom types

Downloaded from jpet.aspetjournals.org at ASPET Journals on April 4, 2018

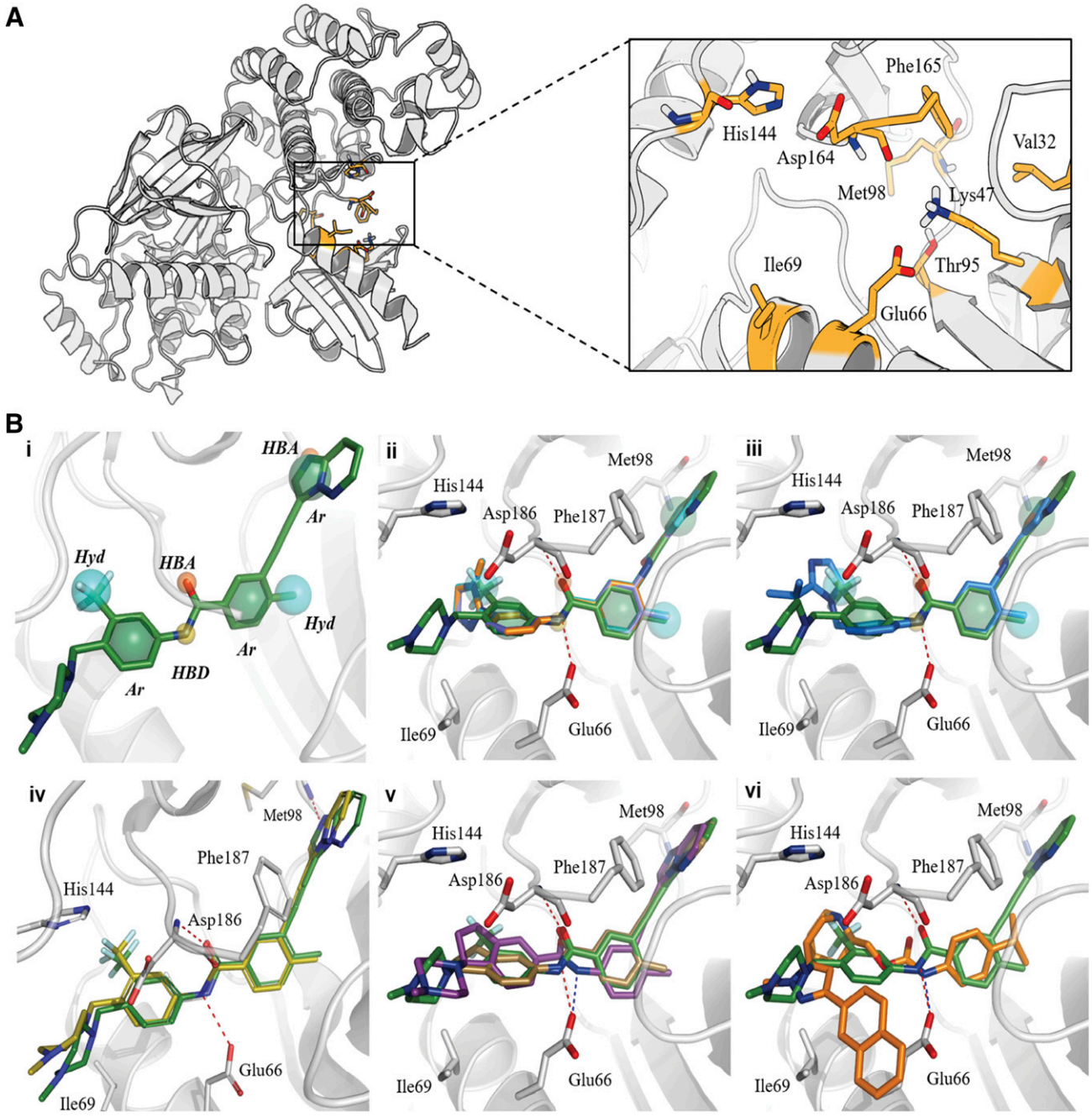

Fig. 1. (A) Schematic of the RIPK2 active site. (B) Representation of pharmacophore points: hydrogen bond donor (HBD, yellow), hydrogen bond acceptor (HBA, orange), hydrophobic (Hyd, cyan) and aromatic (Ar, green). Predicted binding modes of ponatinib (green) (i), MolPort-016-359-762 (orange) (ii), and MolPort-016-412-727 (blue) (iii) in the RIPK2 binding site. (iv) Comparison between the binding position of ponatinib found within the crystal structure (yellow) and the binding mode predicted by AutoDock Vina (green). Predicted binding modes of PC_57410628 (purple), PC_68349611 (brown) (v), and PC_44716361 (MolPort-001-746-327, orange) (vi) in the RIPK2 binding site. All hydrogens were omitted for clarity. The dotted lines represent distances for the formation of hydrogen bonds.

needed for the calculation. A total of nine runs were performed with an exhaustiveness of 50. The best binding mode of each molecule was selected based on the lowest binding free energy score. The three-dimensional figures were generated using PyMOL Molecular Graphics System (DeLano Scientific LLC, Palo Alto, CA).

RIPK2 In Vitro Kinase Assay. For this protocol, samples were lysed in 1× RIPK2 lysis buffer [50 mM Tris (pH 7.5), 0 mM $MgCl_2$, 1% Triton X-100, 1 mM dithiothreitol, 1 mM EDTA, 1 mM EGTA, with freshly added 1 mM β-glycerophosphate and protease inhibitors (phenylmethylsulfonyl fluoride and aprotinin)] and immunoprecipitated overnight using 1.5 μg rabbit anti-RIPK2 antibody. The next day, protein G sepharose was used to immunoprecipitate the RIPK2 protein complex immunoprecipitation (IP) for 1.5 hours. Following this incubation, samples were washed once in 1× kinase wash buffer [50 mM Tris (pH 7.5), 150 mM NaCl, 1% Triton X-100, 1 mM EDTA] followed by two washes with 1× kinase buffer [30 mM Hepes (pH 7.5), 10 mM $MgCl_2$, 2 mM $MnCl_2$]. After the last wash, 20 μl of water was added to beads, followed by 1× kinase buffer and ^{32}P-γ-ATP, and kinase reaction was allowed to proceed for 45–60 minutes at 30°C. Protein loading dye was added to the mix,

Downloaded from jpet.aspetjournals.org at ASPET Journals on April 4, 2018

TABLE 1
Calculated binding free energies of potential RIPK2 inhibitors
ZINC, MolPort, and PubChem (PC) molecule identification numbers are shown. MolPort-016-359-762 is RIPK2 inhibitor 1 and PC_44716361 (MolPort-001-746-327) is RIPK2 inhibitor 2.

Compound	ΔG_{bind} kcal/mol	Compound	ΔG_{bind} kcal/mol
Pharmacophore			
Ponatinib	−11.9	MolPort-015-604-588	−10.6
MolPort-016-359-762	−11.5	MolPort-016-412-727	−10.6
MolPort-015-752-252	−10.8	ZINC02739307	−10.1
Structure similarity			
PC_57410628	−12.0	PC_58945682	−11.5
PC_44716361	−11 8	PC_58945685	−11.5
PC_24826801	−11 8	PC_68349611	−11.5
PC_57405602	−11.6	PC_58945669	−11.3
PC_58945635	−11.6	PC_40780119	−11.1

and samples were boiled and separated on an SDS-PAGE gel. The gel was dried and then exposed to X-ray film to capture the autophosphorylation of RIPK2.

NFκB Gene Reporter Luciferase Assay. The Dual-Luciferase Reporter Assay System (E1910; Promega, Madison, WI) was used to perform dual-reporter assays on NFκB luciferase and Renilla luciferase (internal control). In brief, HCT116 colon cancer cells were equally seeded at a density of 3×10^4 in six-well plates and allowed to attach for 24 hours. Prior to transfection, cells were washed with serum-free medium three times. Dual transfection was carried out using 12 μl of polyethylenimine to 3 μg of NFκB luciferase construct and 60 ng of Renilla luciferase construct. Twenty-four hours after transfection, cells were treated with the different drugs for 24–36 hours. Cells were then lysed using the passive lysis buffer provided by the kit for 30 minutes on ice. Lysate was spun down for 8 minutes at 10,000 rpm, and 20 μl of cell lysate was transferred into a 96-well plate. Luciferase assays were analyzed based on the ratio of Firefly/Renilla to normalize cell number and transfection efficiency.

Intestinal Inflammation Injury Model. Animals were administered 3% (w/v) dextran sulfate sodium (DSS; molecular weight of 40,000–50,000; MP Biomedicals, Santa Ana, CA) in the drinking water for 7 days followed by recovery for 7 days. They were monitored for piloerection, bloatedness, tremors, lack of movement, rectal bleeding, and weight loss [all on a scale of 0–5, with 5 being very severe; adapted from Madsen et al. (2001)]. Animals were euthanized once rectal bleeding became grossly apparent. For weight loss, the following scores were assigned: 0 for no weight loss, 1 if 5% loss, 2 for 5%–10% loss, 3 for 10%–15% loss, 4 for 15%–20% loss, and 5 for >20% loss in initial body weight. Disease activity indices were the sum of all individual scores. All animals were male of the C57BL/6 background and at 10–12 weeks of age or 25 g in body weight at the beginning of the experiment.

Lung Inflammation Model. Male Balb/c mice (6–8 weeks) were sensitized on days 1 and 6 via intraperitoneal injection of 0.9% sterile saline (0.5 ml) or 0.9% saline containing 10 μg of ovalbumin and 2 mg of $Al(OH)_3$. After light anesthesia with ketamine (75 mg/kg) and acepromazine (2.5 mg/kg), mice were challenged intranasally with 25 μl of saline containing 50 μg of ovalbumin or saline alone as a control on days 12 and 14. RIPK2 inhibitor 1 (1 μg/g body weight) or 30% dimethylsulfoxide (DMSO; solvent control for drug) was injected intraperitoneally on days 12, 13, and 14 (on days 12 and 14, the injection was performed 1 hour before the intranasal challenge with ovalbumin). On day 15, mice were euthanized with an intraperitoneal injection of 2 mg of sodium pentobarbital. Cardiac puncture was used to collect blood, followed by tracheal intubation with polyethylene tubing. The lungs were washed twice, with 1 ml of phosphate-buffered saline, pH 7.4, and 2 ml of bronchoalveolar lavage (BAL) fluid was collected. BAL fluid was spun at 300*g* for 5 minutes. Cell pellets were resuspended in phosphate-buffered saline, total cell count was performed, and then cytospins were prepared with 5000 cells. The slides were stained with Diff-Quick (Polysciences, Warrington, PA), and differential cell counts were performed to assess allergic airway inflammation. This was done in collaboration with Dr. Harissios Vliagoftis (University of Alberta, Edmonton, AB, Canada).

Mass Spectrometry. Direct-infusion measurements were carried out on an LTQ Orbitrap XL mass spectrometer (Thermo Fisher Scientific, Waltham, MA) using the Ion Max ESI source (Thermo Fisher Scientific). The on-board syringe pump was used with a 100-μl Hamilton syringe and a flow rate of 5 μl/min. The following parameters were used: sheath gas flow of 15 arbitrary units, auxiliary gas flow of 5 arbitrary units, spray voltage of 3.5 kV, tube lens voltage of 110 V, capillary temperature of 275°C, capillary voltage of 35 V, and capillary temperature of 275°C. The automatic gain control target was set to $1e^6$ and the maximum injection time to 200 ms. The resolution was set at 100,000, and two microscans were recorded.

NMR Spectroscopy. NMR experiments were run on a Varian Inova 500 MHz spectrometer (Agilent, Santa Clara, CA) at 30°C. The proton chemical shifts were measured relative to the residual protonated methyl (CHD_2) signal of d_6-DMSO (2.50 ppm); coupling constants (J) are reported in Hz. Standard notation is used to describe the multiplicity of signals observed in ^{1}H NMR spectra: singlet (s), doublet (d), triplet (t), broad (b), etc. Through-space and through-bond connectivities were observed using a two-dimensional ^{1}H-^{1}H rotating-frame Overhauser enhancement spectroscopy (^{1}H-^{1}H ROESY) experiment (mixing time 200 ms). One-dimensional experiments were processed using VNMRJ (Varian Associates, Palo Alto, CA), and two-dimensional ^{1}H-^{1}H ROESY was processed using NMRPipe/NMRDraw software (Ad Bax group, Bethesda, MD). RIPK2 inhibitor 1 was prepared by dissolving 0.3 mg in 500 μl d_6-DMSO. RIPK2 inhibitor 2 was prepared by dissolving 0.3 mg in 500 μl of d_6-DMSO (Delaglio et al., 1995).

Use of Animals. All animal experimentation was performed in accordance with the University of Alberta institutional guidelines as defined by the Animal Care and Use Committee.

Statistical Analysis. Statistical analysis was carried out by analysis of variance and Student's *t* test (two-tailed) as indicated.

Results

Pharmacophore Search. The ponatinib/RIPK2 complex (PDB: 4C8B) has revealed significant binding interactions of this inhibitor in the RIPK2 active site. Based on this crystal structure, the active site is localized in a binding pocket formed by at least eight different amino acid residues, including Val32, Lys47, Glu66, Ile69, Leu70, Thr95, Met98, and Asp164 (Fig. 1A). In this work, the ZINC and MolPort databases were screened with the ZINCPharmer pharmacophore search server using the lead drug Ponatinib as a query. Several pharmacophoric features were identified directly from the RIPK2 structure and used for the screening. In this regard, a total of 74 compounds were identified from both databases with pharmacophoric points similar to ponatinib (Fig. 1B). The compounds were then docked into the same RIPK2 binding site in which ponatinib is located. Interestingly, 54 compounds shared the pharmacophore distribution of ponatinib. Table 1 summarizes the docking scores of the compounds with the lowest binding free energies. Figure 1B shows the location of the pharmacophoric points identified for the interaction of ponatinib with the RIPK2 active site and the proposed binding modes of the ligands with the lowest binding free energies, respectively. It is noteworthy that the compounds with the lowest calculated binding free energies exhibit a high structural similarity between them [MolPort-016-359-762 (labeled as RIPK2 inhibitor 1 in subsequent

Downloaded from jpet.aspetjournals.org at ASPET Journals on April 4, 2018

figures, 3-benzamido-4-methyl-*N*-[3-(1-methyl-1H-imidazol-2yl)phenyl]benzamide), MolPort-015-752-252, MolPort-015-604-588, and MolPort-016-412-727) and a high correlation with pharmacophoric points of ponatinib. These results suggest that compound MolPort-016-359-762 and its derivatives have a high probability of inhibiting RIPK2.

Structure Similarity Search. A total of 10,655,787 compounds with at least 60% similarity to ponatinib were obtained from the PubChem database to dock them into this binding site and identify new potential inhibitors. We selected the most similar (≥90%; 803 compounds) and less similar (<62%; 50,000 compounds randomly selected from a total of 2,607,266) structures to identify ponatinib-like molecules and novel scaffolds, respectively. After filtering with Lipinski's rule and removing duplicates and inorganic molecules, we performed molecular docking studies in the RIPK2 active site using AutoDock Vina, from which more than 500 compounds with a calculated ΔGbind ≤−10.0 kcal/mol were identified. The docking scores of ponatinib and the compounds with the lowest binding free energies are summarized in Table 1. As might be expected, the compounds with the highest similarity in values showed similar binding modes compared with ponatinib (PC_24826801, PC_57405602, PC_58945635, PC_58945682, and PC_58945685). However, compound PC_57410628 was the only molecule with a lower binding free energy than the lead molecule. Moreover, compound PC_44716361 [MolPort-001-746-327 (labeled as RIPK2 inhibitor 2 in subsequent figures)], which presents a lower similarity to ponatinib, represents a new scaffold with unique structural features offering alternatives from a medicinal chemistry perspective. Figure 1B shows the proposed binding mode of these ligands in the RIPK2 binding site. This figure also shows that all of the compounds identified possible form hydrogen bonds between the Glu66 residue and the carboxamide group. The initial virtual screening, ranking chemical structures, and the pan-assay interference compounds check of the selected compounds (Sterling and Irwin, 2015) are reported in Supplemental Table 1.

Utilizing mass spectrometry and ^{1}H-NMR (Fig. 2; Supplemental Figs. 1–3A), we confirmed >95% purity of our two lead compounds and confirmed the structure of the identified RIPK2 inhibitors 1 and 2. ROESY spectra provided through-bond and through-space connectivities that were essential for obtaining complete chemical shift assignments of both molecules (Supplemental Figs. 1 and 2). In addition, through-space rotating-frame nuclear Overhauser enhancement (ROE) connectivities provided valuable information about the conformational preferences of RIPK2 inhibitor 1 in solution (Fig. 2B). The lack of ROEs between HN22 and either HC17 or HC25 indicates that the central methyl-containing aromatic ring is roughly perpendicular to the amide plane of HN22, as would be expected based on steric considerations. In contrast, HN13 shows ROEs to HC8, HC17, and HC21, indicating that the two central benzene rings are more planar with respect to the central amide bond of HN13, similar to the conformation seen in ponatinib (Fig. 1B). Thus, the arrangement of benzene rings found in RIPK2 inhibitor 1 resembles the geometry of the corresponding aromatic rings in ponatinib bound to RIPK2. The presence of both HN13–HC17 and HN13–HC21 ROEs suggests rotation about the C14–C16 bond, with rotomer i (Supplemental Fig. 1B) matching the conformation found in ponatinib-RIPK2. However, the presence of an HN13–HC8 ROE coupled with the absence of an HN13–CH10 ROE suggests that rotation about the C9–N13 bond is more restricted, which may force the imidazole ring of RIPK2 inhibitor 1 into a position opposite to the corresponding CF_3 group of ponatinib-RIPK2 (Fig. 1B, panel iii), which would place it in a more solvent-exposed position than the buried position of the CF_3 group. Further detailed analysis may be warranted to isolate these two forms and determine bioactivities for RIPK2 and NFκB inhibition.

Validation of RIPK2 Inhibitors Using Kinome Analysis. The specificity of the identified RIPK2 inhibitors to inhibit numerous kinases was explored utilizing the Kinome Scan profiling service at DiscoverX (Fremont, CA). This utilizes an in vitro kinase approach with purified recombinant kinases/peptide substrates to determine activity of kinases in the panel. We explored if our lead compounds, RIPK2 inhibitors 1 and 2, can inhibit other targets at 100 nM in the 97 kinome panel (Supplemental Table 2A). This concentration was used due to robust inhibition of NFκB and RIPK2 kinase assay in assays outlined in Figs. 2–6. The kinome inhibition analysis revealed robust selectivity toward RIPK2 for RIPK2 inhibitor 1 with 20%–27% inhibition of c-ABL, Aurora kinase B, or ERBB2 (Supplemental Table 2A). RIPK2 inhibitor 2 appears to inhibit 38% of the activity of SNARK and 27% of the activity of FGFR2, GSK3-β, JNK1, CSNK1G2 (casein kinase 1), and MET tyrosine kinase. These off-target inhibitions are not surprising, as it is difficult to obtain a specific small-molecule inhibitor. This would suggest possible activities beyond inhibiting RIPK2 that will need to be empirically tested. Initial empirical testing for c-ABL was carried out via an in vitro kinase approach with purified recombinant kinases at the MRC Protein Phosphorylation and Ubiquitination Unit in Dundee, Scotland. Both of our RIPK2 small-molecule lead compounds inhibited c-ABL but with an IC_{50} of >100 μM (Fig. 3A). Given this observation, we hope that the off-target effects on Aurora kinase B and ERBB2 (if any) will also be in a vastly different concentration range of 100 nM.

Cell-Based Confirmation of RIPK2 Inhibition and Inhibition of NFκB Activation. We next explored cell-based in vitro inhibition of RIPK2. We can clearly observe RIPK2 inhibitor 1 and 2 inhibition of MDP-dependent activation of RIPK2 autophosphorylation (on tyrosine 474) using an in vitro kinase assay in HCT116 cells (Fig. 3B). MDP is the molecular ligand for the NOD2 pathogen receptor whereby RIPK2 can be activated. Similar results for RIPK2 inhibitor 1 inhibition of RIPK2 were obtained in breast cancer cells (BT549 and MDA-MB231 cells, data not shown). Immunodepletion using an anti-RIPK2 antibody (Fig. 3C, condition B) or Crispr/Cas9 knockout of RIPK2 (Fig. 3D) confirmed specificity of detection of the autophosphorylated RIPK2 band in Fig. 3B. Furthermore, using a phospho-tyrosine [Y] 474 (in-house generated) and a phospho-serine [S] 176 (Cell Signaling, Inc., Danvers, MA) RIPK2 antibodies, we confirmed that active RIPK2 is recognized by these antibodies upon activation with MDP treatment in 293HEK fibroblast and HCT116 colon cancer epithelial cells (Fig. 3E, left panel) and detection of constitutively active RIPK2 in the colon cancer cell line SW480 (Fig. 3E, right panel). Interestingly, we can observe constitutively active RIPK2 in Hodgkin's lymphoma cell lines HDMYZ, L428 (Fig. 4A), and KMH2 cells (Fig. 4B). This signal

Downloaded from jpet.aspetjournals.org at ASPET Journals on April 4, 2018

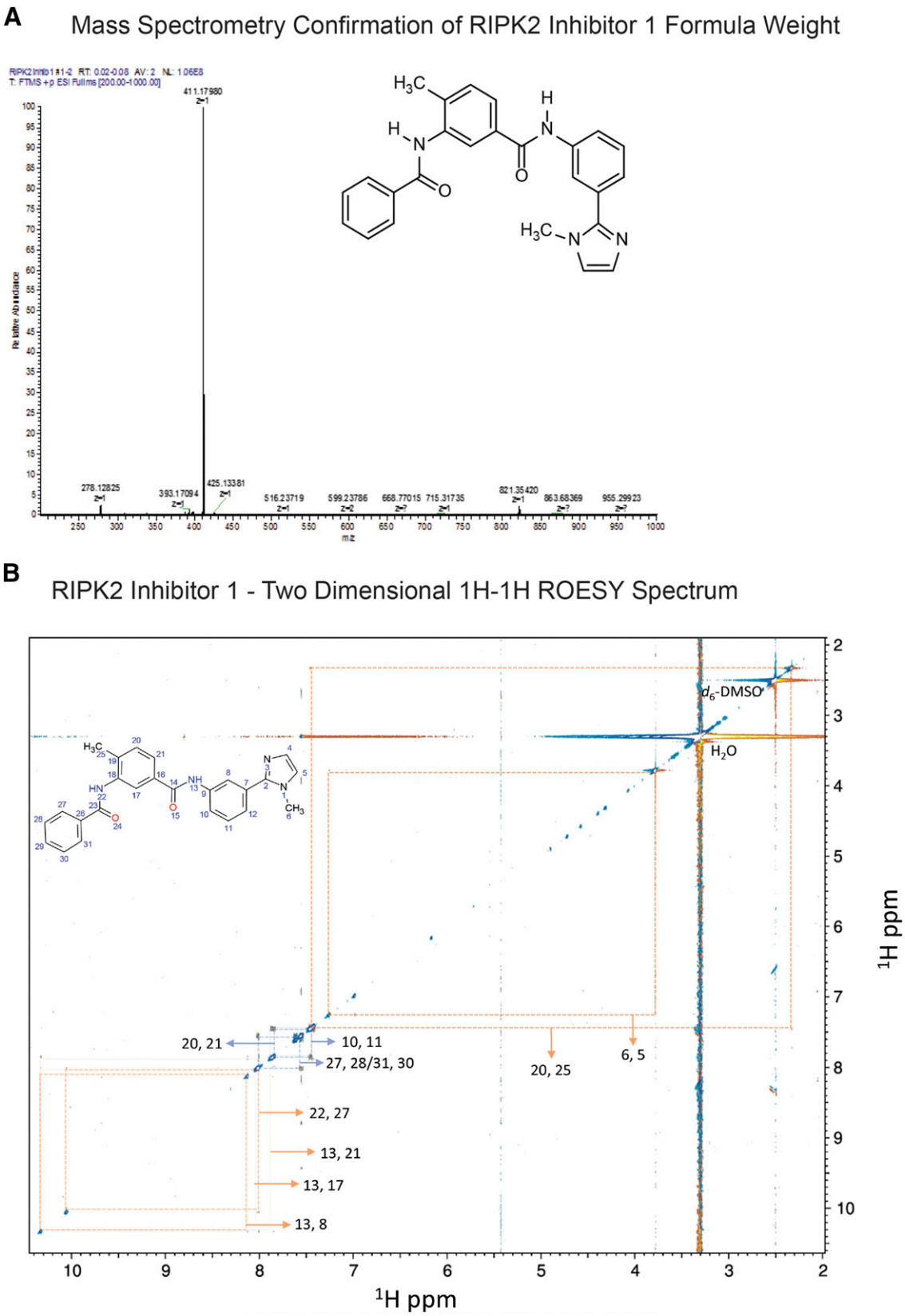

Fig. 2. Mass spectrometry and NMR confirmation of mass and structure of RIPK2 Inhibitor 1. (A) Direct-infusion measurements were carried out on an LTQ Orbitrap XL (Thermo Scientific) mass spectrometer using the Ion Max ESI source. Mass confirmation was obtained as indicated. (B) Two-dimensional ^{1}H-^{1}H ROESY spectrum of 3-benzamido-4-methyl-*N*-[3-(1-methyl-1H-imidazol-2-yl)phenyl]benzamide. Boxes (orange) represent through-space connectivities between protons in the compound. Blue boxes are signals due to three-bond *J*-coupling between aromatic ring protons. Four-bond *J*-coupling signal is less intense. AV, number of scans that were averaged; FTMS, Fourier Transform Mass Spectrometry; NL, normalized level; RT, retention time.

Downloaded from jpet.aspetjournals.org at ASPET Journals on April 4, 2018

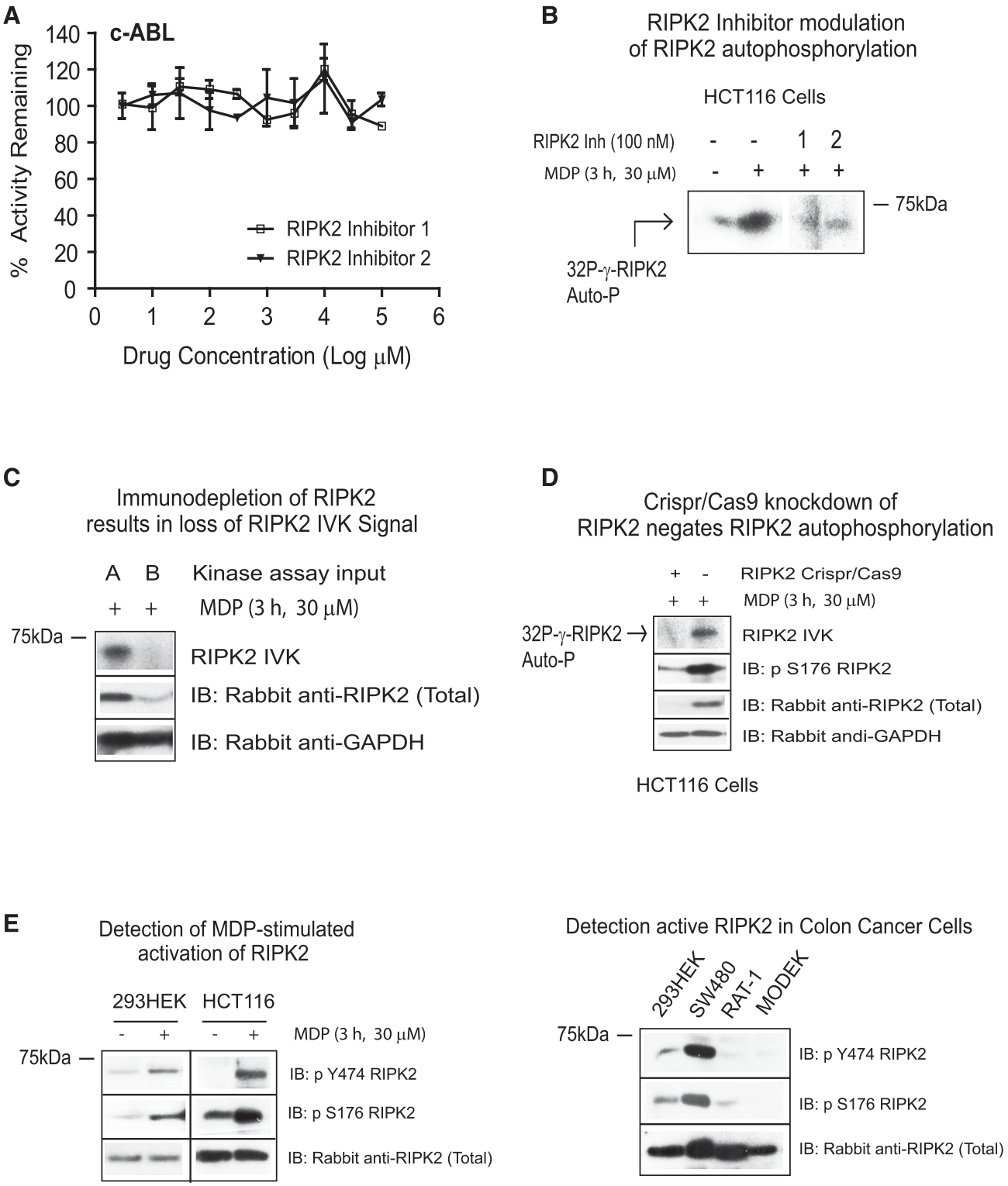

Fig. 3. Analysis of RIPK2 kinase activity. (A) Kinase activity for c-ABL was tested in the presence of inhibitors 1 and 2. IC_{50} for c-ABL for both inhibitors is >100 μM. Analysis was carried out using purified c-ABL and the substrate peptide, EAIYAAPFAKKK, in association with the MRC Unit on Phosphorylation and Ubiquitination, University of Dundee, Scotland. (B) RIPK2 autophosphorylation (Auto-P) at site Y474 is shown. Inhibition was carried out on cells followed by lysis and IP with rabbit anti-RIPK2 overnight. Following protein G pull down and wash, ^{32}P-γ-ATP was added and kinase reaction was allowed to proceed for 30 minutes at 30°C. Following kinase reaction, SDS-PAGE was used to separate out the proteins, and gel was then dried and exposed to film. (C) RIPK2 in HCT116 cells were IP with an anti-RIPK2 antibody (A) and the supernatant after IP in (A) was IP in (B) with the same RIPK2 antibody, and in vitro kinase (IVK) assay was carried out on both samples. (D) Crispr/Cas9 knockout of RIPK2 in HCT116 colon cells was carried out, followed by MDP activation and RIPK2 IVK analysis to illustrate use of RIPK2 Crispr/Cas9 reagents and specificity of our IVK assay. (E) Left panel: cells were stimulated with MDP for 3 hours, and RIPK2 activation was monitored by a phosphotyrosine (pY) 474 RIPK2 antibody (in-house antibody) and phosphoserine (pS)176 phosphorylation (Cell Signaling). Right panel: several colon cancer cells were investigated for constitutive activation of RIPK2 using phosphorylation specific antibodies to pY474 and pS176 as indicated. Bottom: constitutive activation of RIPK2 in numerous cell lines are explored. GAPDH, glyceraldehyde-3-phosphate dehydrogenase; IB, immunoblotting.

Downloaded from jpet.aspetjournals.org at ASPET Journals on April 4, 2018

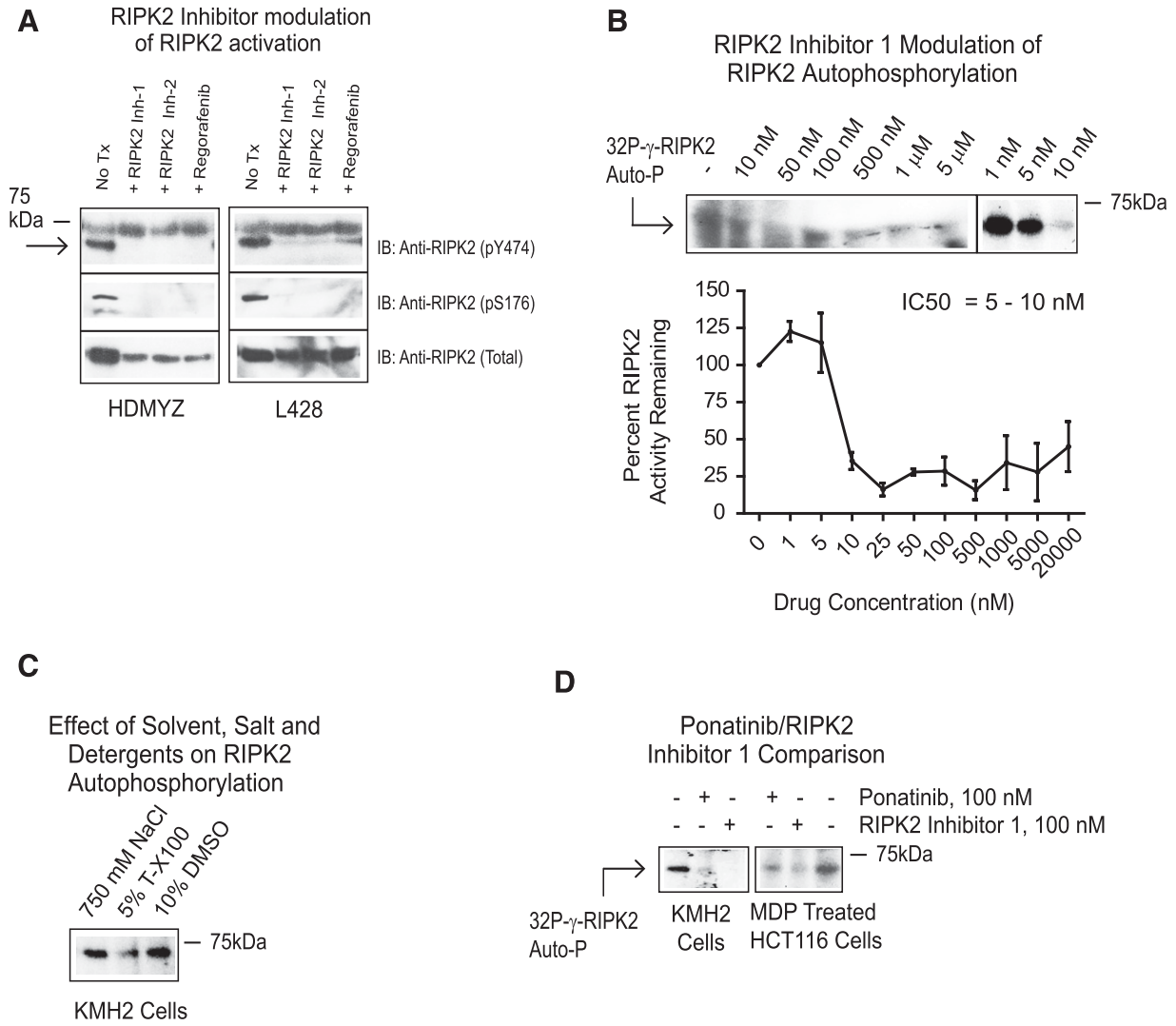

Fig. 4. Characterization of RIPK2 kinase inhibitors. (A) Immunoblot illustration of the use of RIPK2 phospho-antibodies in two Hodgkin's lymphoma cells that have constitutive active RIPK2. A comparison with a known RIPK2 inhibitor is shown (regorafenib). All inhibitor concentrations were 100 nM. Similar results were observed for a third Hodgkin's lymphoma cell line, KMH2 [see (B)]. (B) KMH2 Hodgkin's lymphoma cells were inhibited in vivo for 33–36 hours using the indicated concentration of RIPK2 inhibitor 1. (Top) An in vitro kinase assay was carried out by IP overnight with 1 μg of the rabbit anti-RIPK2 antibody from ProteinTech (Rosemont, IL) and 1 ml of lysate from a confluent six-well dish of KMH2 cells. Immune complexes were separated by SDS-PAGE and captured by autoradiography. (Bottom) Quantitation of three to five independent experiments to reveal an approximate IC_{50} of 5–10 nM for in vivo RIPK2 inhibition. (C) Analysis of effect of drug solvent (DMSO), salt concentration, and detergents on the kinase activity of RIPK2. Following IP, the indicated reagents were added for 10 minutes followed by 32-γ-ATP to initiate the kinase reaction as described in the *Materials and Methods* section. (D) RIPK2 in vitro kinase assay was carried out as in Fig. 3B in KMH2 and HCT116 cells in the presence of ponatinib or RIPK2 inhibitor 1 to carry out a comparison of RIPK2 inhibition. IB, immunoblotting.

can effectively be inhibited using RIPK2 inhibitors 1 and 2 and regorafenib (a known RIPK2 kinase inhibitor) at 100 nM as determined using RIPK2 phospho-specific antibodies (Fig. 4, A and B). Furthermore, we determined that RIPK2 inhibitor 1 effectively inhibited KHM2 cells at an approximate IC_{50} of 5–10 nM, and kinase activity was somewhat sensitive to detergent conditions (Fig. 4, B and C). When compared with inhibition with ponatinib (a known RIPK2 inhibitor and chemical template for selecting our RIPK2 small molecule), our RIPK2 inhibitor performed equally to inhibit RIPK2 kinase activity in an in vitro kinase assay in two different cell lines (Fig. 4D).

The functional consequence of inhibiting MDP-dependent activation of RIPK2 is the loss of NFκB activity (Fig. 5; Supplemental Fig. 3B) and DNA binding ability, especially for the interleukin-8 (IL-8) promoter (Supplemental Fig. 4A). Not surprisingly, RIPK2 inhibitor 1 was more efficacious at 100 nM at inhibiting NFκB activity when compared with RIPK2 inhibitor 2, gefitinib, or regorafenib (*P* values comparing RIPK2 inhibitor 1 vs. RIPK2 inhibitor 2, gefitinib, and regorafenib inhibition of MDP-driven NFκB activation were 0.0015, 0.0006, and 0.004, respectively). However, RIPK2 inhibitor 1 was as efficacious as ponatinib at 100 nM for NFκB inhibition (*P* value = 0.06 when comparing RIPK2 inhibitor 1 vs. ponatinib inhibition of MDP-driven NFκB activation). Interestingly, a recently characterized RIPK2 inhibitor, GSK-583 (Haile et al., 2016), did not inhibit MDP-dependent NFκB activity at 100 nM in HCT116 cells (data not shown), although it is known to in primary immune cells. Interestingly, we did observe a small but significant

Downloaded from jpet.aspetjournals.org at ASPET Journals on April 4, 2018

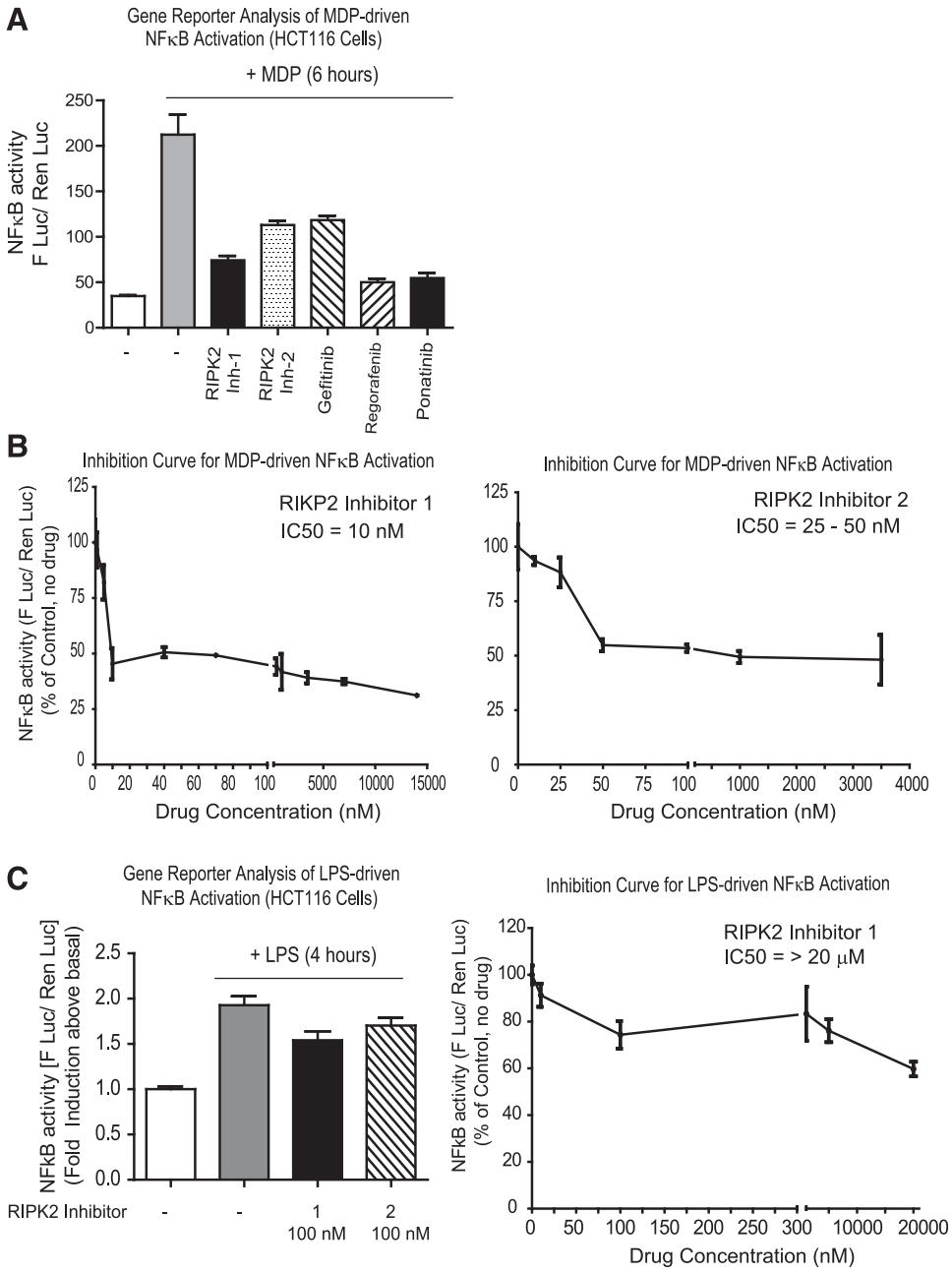

Fig. 5. RIPK2 Inhibition of NFκB activity. (A and B) NFκB gene reporter assay determination of inhibition of MDP-stimulated NFκB activity with RIPK2 inhibitors (A) and an approximate IC_{50} determination for inhibition of MDP driven-NFκB activation using RIPK2 inhibitors 1 and 2 (B). All drugs in (A) were used at 100 nM. *P* values for RIPK inhibitor treated vs. MDP (no drug) were <0.0001 (inhibitor 1), 0.06 (inhibitor 2), <0.006 (gefitinib), 0.0002 (regorafenib), and 0.0008 (ponatinib). For ponatinib, $n = 4$ and $n = 10$ for the rest with approximate IC_{50} curves shown in (B). (C) Left panel: NFκB gene reporter assay determination of inhibition of LPS-stimulated NFκB activity with RIPK2 inhibitors (concentration as indicated). *P* values for RIPK2 inhibitor treated vs. LPS (no drug) were <0.02 (inhibitor 1) and <0.268 (for inhibitor 2) ($n = 6$). Right panel: approximate IC_{50} determination for inhibition of LPS-NFκB–driven inflammation using RIPK2 inhibitors 1 and 2 (B).

reduction in lipopolysaccharide (LPS; via TLR4 and TLR2), TNFα, and IL-1β–dependent activation of NFκB (Fig. 5C and an approximate IC_{50} in Fig. 5C, right panel; Supplemental Fig. 3B). Although a reduction, the approximate IC_{50} for RIPK2 inhibition of LPS-driven NFκB activation is >20 μM, and we speculate it will also be much higher for inhibition of TNFα and IL-1β–dependent activation of NFκB. Interestingly, RIPK2 inhibitor 1 can also inhibit the activation of hypoxia-response element I response to chemical induction using 1% H_2O_2 (Supplemental Fig. 3C) to suggest either a link to inflammation or a direct modulation of hypoxia-inducible factor α function. These observations validate the specificity of our RIPK2 inhibitor for NOD/RIPK2 biology and usefulness as an in vivo inhibitor of MDP-driven inflammation.

RIPK2 Inhibitors Can Inhibit the Proliferation of Several Cancer Cells but Do Not Promote Apoptosis or Cell Cycle Arrest. Inflammation is a strong driver of malignant transformation and abnormal proliferation, especially in the colon (Lasry et al., 2016) and breast (Suman et al., 2016). We explored the ability of RIPK2 inhibitors to reduce the proliferative rate of highly metastatic cancer cells. For most of the cancer cells, 45–100 nM RIPK2 inhibitor 1 inhibited >70% of the proliferation of colon and blood cancer cells while preserving the proliferation of normal Rat-1 and ModeK intestinal epithelial cells (Fig. 6A). These data would suggest strong suppressive properties of RIPK2 inhibitor 1 and, to some extent, inhibitor 2 on cell proliferation. Regorafenib, a recently characterized RIPK2 inhibitor, did not significantly inhibit the proliferation of these cells in an

Downloaded from jpet.aspetjournals.org at ASPET Journals on April 4, 2018

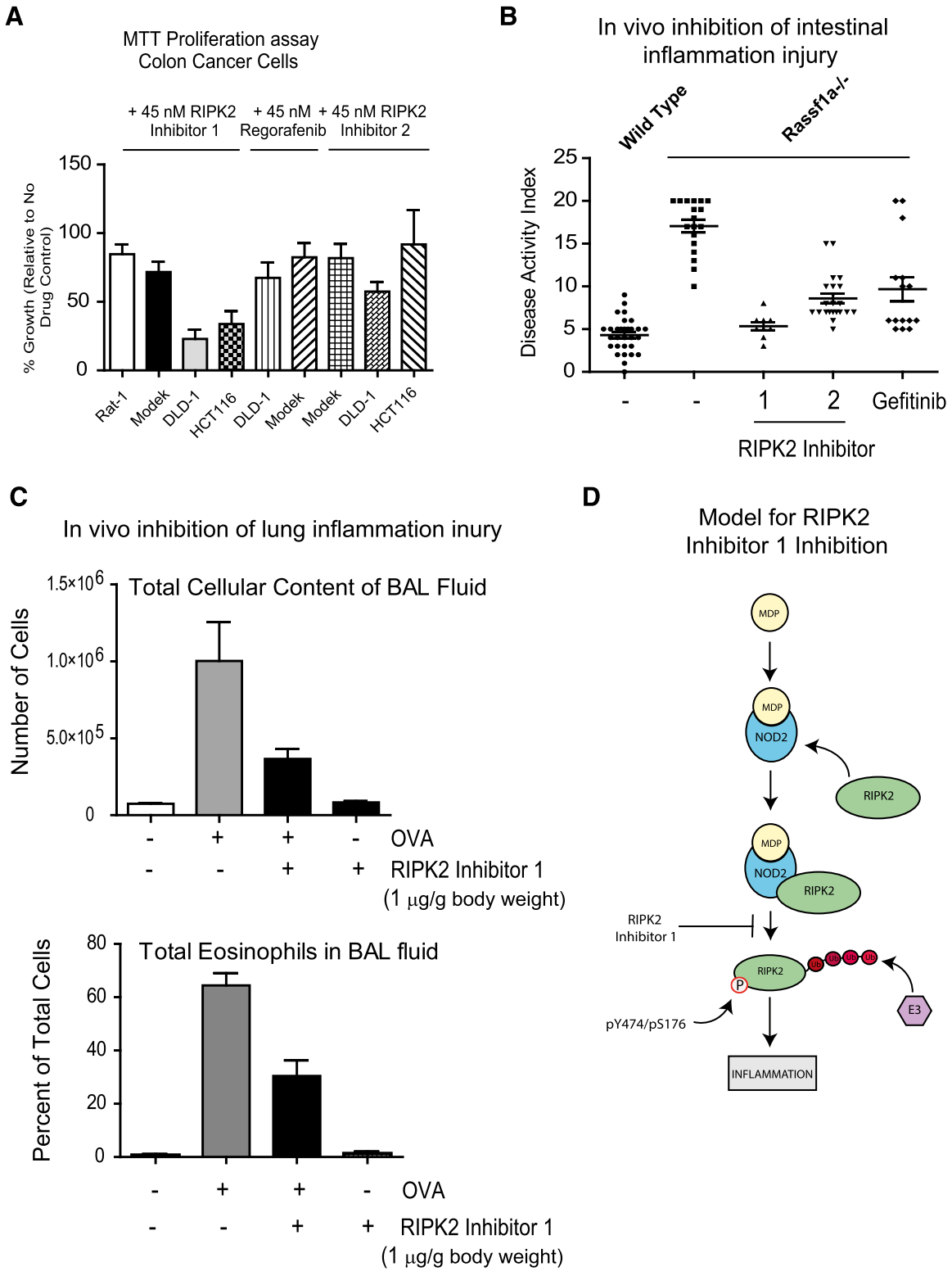

Fig. 6. In vivo inhibition of proliferation, intestinal, and lung inflammation using RIPK2 inhibitors. (A) RIPK2 inhibitors modulate the proliferation of several colon cancers but not normal cells. MTT assay was carried out with the indicated concentrations of RIPK2 inhibitors in the indicated cell lines. HCT116 and DLD-1 are colon cancer cell lines, whereas RAT-1 and MODEK are normal rat and mouse intestinal cell lines, respectively. RIPK2 inhibitor 1 does not appear to interfere with proliferation of normal intestinal cells (Rat-1 and ModeK) at 45 nM. For all experiments, $n = 5–29$. P value of HCT116 (+ inhibitor 1) vs. HCT116 (+ inhibitor 2) was <0.03; DLD-1 (+ inhibitor 1) vs. DLD-1 (+ inhibitor 2) was <0.02; DLD-1 (+ inhibitor 1) vs. DLD-1 (+ regorafenib) was <0.006. For RIPK2 inhibitor 1–treated DLD-1 or HCT116 vs. RIPK2 inhibitor 1–treated ModeK or Rat-1 cells (normal cells), $P < 0.002$ (analysis in either cell type); for RIPK2 inhibitor 2–treated DLD-1 or HCT116 vs. RIPK2 inhibitor 2–treated ModeK cells (normal cells), $P < 0.02$ and 0.098 (analysis in DLD-1 or HCT116 cells, respectively); for regorafenib-treated DLD-1 vs. regorafenib-treated ModeK (normal cells), $P < 0.2$ but >0.05. (B) Intestinal inflammation injury was carried out using the DSS model. DSS is taken up in the drinking water and migrates to the colon to cause irritation and localized inflammation. *Rassf1a*$^{-/-}$ mice are extremely sensitive to this model, with $<25\%$ survival following a 3% DSS insult for 7 days followed by water for 7 days. Most *Rassf1a*$^{-/-}$ mice require euthanasia by days 7–9. Disease activity is scored based on rectal bleeding, piloerection, movement, and

Downloaded from jpet.aspetjournals.org at ASPET Journals on April 4, 2018

TABLE 2
Survival of *Rassf1a*$^{-/-}$ animals during DSS-induced inflammation
The presence of RIPK2 inhibitors reduced acute intestinal inflammation and enhanced overall survival of the mice.

RIPK2 Inhibitor	Treatment and Genotype	Percentage Survival
No drug	DSS-treated *Rassf1a*$^{-/-}$	7/30 = 22%
1 (MolPort-016-359-762)	DSS-treated *Rassf1a*$^{-/-}$	8/11 = 73%
2 (MolPort-001-746-327)	DSS-treated *Rassf1a*$^{-/-}$	5/9 = 56%
Gefitinib	DSS-treated *Rassf1a*$^{-/-}$	7/15 = 47%

MTT assay (3-(4,5-dimethylthiazol-2-Yl)-2,5-diphenyltetrazolium bromide) (Fig. 6A). We also observed inhibition of triple negative breast cancer cells, HCT1143 and MDA-MB231, with RIPK2 inhibitor 1 (Supplemental Fig. 4B), suggesting effective antiproliferative properties. The approximate IC_{50} for inhibition was around 30–60 nM for most of the cells tested (two are shown in Supplemental Fig. 4C). This effect on growth inhibition was not due to alterations in cell cycle (Supplemental Fig. 5) nor a significant increase in the apoptotic cell populations, suggesting that RIPK2 inhibition of proliferation is independent of cell cycle or apoptotic changes.

RIPK2 Inhibitors Do Not Inhibit RIP1-Directed Cell Death, Ferroptosis, or Modulation of Mitochondrial Physiology. The RIPK family of proteins are actively involved in numerous cell-death processes beyond death receptor–dependent cell death (Vanden Berghe et al., 2016). We characterized two forms of cell death involving erastin-stimulated ferroptosis (an iron-dependent form of cell death, Supplemental Fig. 6A) and VAD-fmk, Smac Mimetic-164, and TNFα stimulation of RIPK1-directed cell death (Supplemental Fig. 6B). In both cases, RIPK2 inhibitor 1 did not interfere with these forms of cell death to support our cell-cycle effects and to suggest no overlap with RIPK1 biology (Supplemental Fig. 6A). Recently, RIPK3 was demonstrated to require a Bax/Bak effect on the mitochondrial permeability transition pore to carry out necroptosis, and the importance of both RIPK1 and RIPK3 in relation to necroptosis-directed degenerative, inflammatory, and infectious diseases has been published (Moriwaki et al., 2015). We thus explored how the identified RIPK2 inhibitors can perturb mitochondrial physiology by evaluating the activity of the sirtuins, a class of deacetylases that use NAD^+ to remove acetyl groups from proteins (Tang, 2016). Indeed, the putative SIRT1 activator resveratrol can stimulate mitochondrial biogenesis to promote increased wellness in the individual (Ostojic, 2017). Therefore, we explored the effect on sirtuin activity using the BIOMOL assay (Enzo Life Sciences, Farmingdale, NY) as described previously (Dai et al., 2016). We observed no statistically significant increase in SIRT1 activation when using the compounds at 0.1 or 10 μM, indicating that phenotypes observed for the use of RIPK2 inhibitors at these doses in cells are likely through SIRT1-independent mechanisms when compared with the effect of resveratrol (Supplemental Fig. 6C). The identified RIPK2 inhibitors are thus selective inhibitors of RIPK2-dependent NFκB pathways if we consider the data in Fig. 5 and Supplemental Figs. 3B, 4, and 5.

RIPK2 Inhibitors Can Efficiently Resolve Intestinal Inflammation in an Ulcerative Colitis Model. DSS-induced intestinal inflammation is a model for ulcerative colitis [a form of inflammatory bowel disease (IBD)]. DSS functions to irritate the colonic mucosa to promote localized inflammation, active cell death, and localized destruction of the epithelial barrier to the lumen of the colon (Dieleman et al., 1998). These events subsequently drive inflammation damage indicative of what IBD patients encounter. NOD2 mutations have been observed in IBD patients, lending support for dysregulated NOD2/RIPK2 signaling driving inflammation in IBD patients (Branquinho et al., 2016). We have demonstrated the importance of Ras association domain *f*amily protein 1A [RASSF1A (or 1A)] in the pathogenesis of colitis in a rodent model (Gordon et al., 2013). RASSF1A is a tumor suppressor involved in TNF-R1–dependent apoptosis, cell cycle control, and restriction of NFκB activation (Gordon et al., 2013). The *Rassf1a* knockout mice (both heterozygous and homozygous forms) are very susceptible to DSS-induced inflammation injury (Gordon et al., 2013) mainly due to uncontrolled inflammation linked to the NOD2/RIPK2 pathway (Said et al., unpublished observation).

Therefore, we carried out intraperitoneal injection of 1 μg/g body weight of RIPK2 inhibitor 1 or 2 on days 5, 7, and 9 to offset the preinflammation damage stage, peak inflammation damage stage, and postinflammation damage/restitution phase. Using this treatment scheme, we observed a robust difference on day 9 in the disease activity indices of wild-type and *Rassf1a* knockout mice that was significantly inhibited with the use of the RIPK2 inhibitors, especially RIPK2 inhibitor 1 (Fig. 6B; Table 2). Interestingly, a newly characterized RIPK2 inhibitor, gefitinib, can also inhibit intestinal inflammation injury but only promote a 41% survival versus 73% survival with RIPK2 inhibitor 1 (Fig. 6B; Table 2). Similar results were obtained for the protein tyrosine kinase inhibitor regorafenib (data not shown). Since both gefitinib and our RIPK2 inhibitors can inhibit RIPK2, either our drug

body weight changes as described previously (Madsen et al., 2001). N = 10–25 and P value of *Rassf1a*$^{-/-}$ (DSS) vs. wild type (DSS) was <0.0001; *Rassf1a*$^{-/-}$ (DSS) vs. *1a*$^{-/-}$ (DSS + inhibitor 1 or 2 or gefitinib) was <0.0001. (C) In vivo inhibition of lung inflammation in an ovalbumin-induced asthma model in mice. Sensitization and challenge with ovalbumin (OVA) in this model induce accumulation of inflammatory cells in the BAL that are primarily eosinophils. Administration of RIPK2 inhibitor-1 significantly decreased both the number of total cells and the number of eosinophils in the BAL fluid (n = 8 for each group). P values for comparison between OVA alone and OVA + RIPK2 inhibitor-1 were 0.019 for total cell numbers and 0.003 for eosinophils. Please note that RIPK2 inhibitor 2 was not used in this experiment due to its higher approximate IC_{50} for NFκB (see Fig. 5B). (D) Model for disruption of NOD2/RIPK2 biology in the presence of RIPK2 inhibitor 1. RIPK2 is activated via tyrosine (Y) (pY474) and serine (S) (pS176) phosphorylation and ubiquitination events to allow for associations with downstream components. RIPK2 inhibitor 1 inhibits phosphorylation at serine 176 and tyrosine 474 and possible inhibition of ubiquitination of RIPK2.

Downloaded from jpet.aspetjournals.org at ASPET Journals on April 4, 2018

has more affinity for RIPK2 or the off-target effects of RIPK2 inhibitor 1 are beneficial to aid in recovery from inflammation injury using the DSS model.

We then explored pharmacokinetic properties of RIPK2 inhibitor 1 in the sera of mice. Analysis revealed that RIPK2 Inhibitor 1 can be eluted at ~3.7 minutes in a region of the chromatogram free of interfering substances (Supplemental Fig. 6D, top panel). After a dose of 1–2 mg/kg IP of inhibitor, the compound was not quantifiable in mouse serum. However, after dosing mice with 15 mg/kg IP, the RIPK2 inhibitor was of measurable concentrations in most of the serum samples assayed. The mean C_{max} was 114 ng/ml occurring at 1 hour after dosing, and the area under the serum concentration versus time curve was 573 ng × h/ml, with a terminal phase half-life of 1.9 hours observed. Therefore, it appears that RIPK2 inhibitor 1 may be efficiently metabolized within 2 hours and cleared from the blood (Supplemental Fig. 6D, bottom panel). Furthermore, toxicity analysis carried out 9 days after the last dose of intraperitoneal injection of 2 μg/g body weight revealed little or no changes in >98% of the markers characterized in a complete blood count (Supplemental Fig. 7). However, creatine kinase activity was significantly elevated in animals treated with RIPK2 inhibitor 1 as opposed to RIPK2 inhibitor 2. During treatment with RIPK2 inhibitor 1 (and post-treatment), we did not overtly observe phenotypic changes in these animals nor notice evidence of health conditions to support a creatine kinase abnormality (such as skeletal muscle defect and movement abnormalities or unexpected euthanasia due to a cardiac abnormality). Interestingly, it has been shown that the creatine/phosphocreatine pathway may play a central role in energy metabolism, and nutritional creatine supplementation has been shown to impart beneficial effects in a number of diverse disease pathologies (Kitzenberg et al., 2016). We speculate this to be the case, as resetting of metabolic abnormalities is needed for recovery of IBD patients who have metabolic syndrome disorder (Goncalves et al., 2015). Further analysis is required to determine if elevated creatine kinase affects the health of the animal, how sustained it is, and if it can be alleviated with RIPK2 inhibitor 1 analogs. In addition, detailed analysis is needed on how our RIPK2 inhibitor 1 is metabolized and removed from the blood, where it accumulates, or if it can cross the blood-brain barrier. These are all unanswered questions that we are currently addressing.

RIPK2 Inhibitors Can Also Efficiently Resolve Lung Inflammation in an Asthma Model. RIPK2 has also been implicated in allergic airway inflammation. RIPK2 gene silencing in the airways decreased allergic airway inflammation in an ovalbumin-mediated mouse model of asthma (Jun et al., 2013). Furthermore, an association between a RIPK2 promoter polymorphism and childhood severe asthma has been shown in a Japanese population (Nakashima et al., 2006). Since we observed robust inhibition of NFκB in the presence of RIPK2 inhibitor 1 and a >70% recovery of animals from DSS-induced inflammation injury (Figs. 4 and 6B), we proceeded to explore the ability to resolve lung inflammation using the ovalbumin challenge model (Kumar et al., 2008). Ovalbumin elicits a robust inflammatory reaction in the airways characterized by an increased number of total cells and eosinophils in the BAL of ovalbumin-sensitized mice (Fig. 6B). In the presence of RIPK2 inhibitor 1 (and, to some extent, with RIPK2 inhibitor 2), we observed a significant reduction in both total cell numbers and eosinophil numbers in BAL fluid. These data suggest effective inhibition of lung inflammation.

Discussion

RIPK2 is the obligate kinase to the NOD2 pathogen receptor pathway and has been demonstrated to be involved in NFκB activation and metastatic behavior in some cancers (Jun et al., 2013) and has a distinct activity versus RIPK1, 3, or 4 (Chirieleison et al., 2016). In addition, several reports suggest involvement in the activation of the immune response upon viral infection (Lupfer et al., 2013) and the requirement for the NOD2/RIPK2 molecular pathway in several models on inflammatory diseases, including experimental colitis (Branquinho et al., 2016) and arthritis (Vieira et al., 2012). Colorectal cancer (CRC) is only one example of a disease that can arise from a prior state of persistent or chronic inflammation. Individuals with IBD and primary sclerosing cholangitis (inflammation of the bile ducts) are at a much higher risk for progressing to CRC and require closer management of their debilitating disease (Dyson and Rutter, 2012; Williamson and Chapman, 2015). As such, therapies to modulate and control inflammation are robust cancer-prevention strategies.

Herein, we performed pharmacophore and similarity-based search and molecular docking studies toward the identification of potential novel RIPK2 inhibitors. In the pharmacophore search, we identified several molecules that share the pharmacophore arrangement with ponatinib. From these, compound MolPort-016-359-762 is one of the most attractive molecules to be tested since it exhibits a high correlation with the pharmacophore model and lowest binding free energy (highest score). Moreover, the similarity-based virtual screening predicted 10 molecules as new potential RIPK2 inhibitors. The lower docking score of one of the less-similar compounds, MolPort-001-746-327, presents a more attractive scaffold to be repositioned as an inhibitor of this enzyme. Interestingly, several analogs of MolPort-016-359-762 also showed higher affinities for the active site pocket of RIPK2, suggesting a high preference of this scaffold for the active site pocket. These analogs may even afford a greater selectivity to inhibit RIPK2 (data not shown). We are currently exploring the use of these analogs of MolPort-016-359-762.

As mentioned earlier, several RIPK2 inhibitors have been characterized. However, like most RIPK2 inhibitors, at 100 nM, OD36 and OD38 can also inhibit 10-FYN protooncogene, transforming growth factor 2 beta, activin receptor like kinase 2, and Lck by >80%. Our identified RIPK2 inhibitors reveal lower binding free energies that other RIPK2 inhibitors identified, suggesting that our inhibitor may be more active. Furthermore, our identified RIPK2 inhibitors appear to have more affinity for the active site of RIPK2 than others, are more efficacious at inhibition of proliferation, and can effectively resolve lung inflammation and intestinal inflammation more robustly than gefitinib (Fig. 6B; Table 2). The efficacious quality of RIPK2 inhibitor 1 in resolving intestinal inflammation may arise from the fact that it can have a small but significant effect on TNFα-, IL-1β-, and LPS-driven NFκB activation as seen in Fig. 5 and Supplemental Fig. 3B. Most inflammatory diseases are complex diseases that have a multitude of inflammatory pathways targeting the area. Thus, to effectively resolve inflammation in these areas,

Downloaded from jpet.aspetjournals.org at ASPET Journals on April 4, 2018

a broad-spectrum inhibitor may be needed to target multiple TLRs and pathogen receptors (Murgueitio et al., 2017).

All of our in vivo inhibition was at 1–2 $\mu g/g$ body weight, which is much lower than the level used for most small-molecule inhibitors. Preliminary pharmacokinetics suggest a 1.89-hour half-life in the blood (Supplemental Fig. 6D), and chronic experiments using RIPK2 inhibitor 1 agree with our preliminary pharmacokinetics, suggesting the efficacious quality of this inhibitor can last for up to 5–6 days after a 1–2-$\mu g/g$ body weight intraperitoneal injection (data not shown). We are currently completing our pharmacokinetic analysis and will be exploring inhibition of intestinal inflammation in the *IL-10*$^{-/-}$ model for inflammatory bowel disease, a model with spontaneous colonic inflammation by 8–10 weeks of age and an established model for IBD (Kuhn et al., 1993).

It has been demonstrated by several groups that RIPK2 has a unique requirement for NOD1 and NOD2 and functions in many pathways different from RIPK1, 3, or 4. Recently, Chirieleison et al. (2016) summarized the uniqueness of RIPK2 kinase domain within the RIPK family that could not be substituted for the kinase domain from RIPK1 or RIPK4. Indeed, RIPK2 inhibitors 1 and 2 did not inhibit RIPK1 biology nor ferroptosis, a form of cell death influenced by proteins of the RIPK family (Supplemental Fig. 6, A and B). As such, we believe that our identified RIPK2 inhibitors 1 and 2 can selectively modulate RIPK2-specific biology in agreement with the observations by Chirieleison et al. (2016).

Although we can observe a robust inhibition of autophosphorylation of RIPK2, NFκB, and alleviation of intestinal and airway inflammation injury in our mouse models of colitis and asthma, our kinome screen demonstrated in vitro inhibition of several other kinases, including 20%–30% inhibition of c-ABL, Aurora kinase B, or ERBB2. We have demonstrated the importance of c-ABL in driving inflammation injury in our acute DSS model in the publication by Gordon et al. (2013). It is likely that our RIPK2 inhibitor 1 may interfere with the kinase activity of these off targets indirectly by resolving the inflammation. Many of these kinases are involved in growth-related pathways, tumorigenesis pathways, and cell cycle control, such as Aurora kinase B (Borisa and Bhatt, 2017). These off-target effects may actually be beneficial in treating IBD, primary sclerosing cholangitis, primary sclerosing cholangitis/IBD-related CRC, and asthma, whereby a multitude of abnormal signaling involving inflammation, oxidative damage, DNA damage, and apoptotic abnormalities exists to manifest itself into a diseased state. Thus, eliminating all of these abnormalities using a single small molecule will promote a return to homeostasis and recovery from inflammation damage. It will be interesting to explore other inflammation states such as obesity, diabetes, cystic fibrosis, psoriasis, and arthritis to determine the importance of RIPK2 in driving inflammation damage and the usefulness of RIPK2 inhibitor 1 to alleviate the clinical symptoms associated with these diseases.

Comparison with Recently Identified RIPK2 Inhibitors. Recently, four inhibitors to RIPK2 were identified as OD36/OD38 (Tigno-Aranjuez et al., 2014) WEHI-435 (Nachbur et al., 2015), GSK-583 (Haile et al., 2016), and the one from Novartis (He et al., 2017). OD36 and OD38 were obtained through a small molecule macrocylization process from Oncodesign (Dijon Cedex, France) with IC_{50} values of < 100 nM and the ability to interfere with MDP dependent RIPK2 activity. WEHI-435 was obtained by analysis of the RIPK2/ponatinib structure and the necrostatin-1/murine RIPK1 structure to obtain a structural face for the murine RIPK2 kinase domain (18–249) (Nachbur et al., 2015). Using this structural face, the computational biology used to obtain small molecules to associate with the RIPK2 ATP-binding pocket, GSK-583, was obtained using structural comparisons of RIPK2 with ponatinib. Last, the Novartis RIPK2 inhibitor was obtained in a similar manner to GSK583 and was based on a proprietary chemical library screen. Several hits were obtained, and after structural optimization, a RIPK2 inhibitor was obtained to inhibit RIPK2 kinase activity at 3 nM (He et al., 2017).

In this study, we used similarity-based virtual screening and molecular docking analysis to identify a RIPK2 inhibitor that can empirically inhibit the autophosphorylation of RIPK2, inhibit NFκB, and alleviate lung and intestinal inflammation efficacious at 1–2 $\mu g/g$ body weight. RIPK2 inhibitors did not inhibit RIPK1 activity involved in ferroptosis or cell death nor have an effect on mitochondrial biology. In addition, RIPK2 inhibitor 1 appeared to also inhibit cell proliferation as determined by MTT assay, which did not appear to promote cell death. We find this curious and will be further exploring how RIPK2 inhibitors 1 and 2 can promote reduced proliferation and interfere with inflammation. Interestingly, RIPK2 has been demonstrated to be involved in the active growth of CD90(+) intestinal stromal cells to suggest an "inflammatory" cross-talk between intestinal stromal cells and the epithelial cells (Owens et al., 2013), and we can observe robust activation of RIPK2 in IBD colon tissue sections immunostained with our proprietary pY474 RIPK2 antibody (Salla et al., unpublished observations). Inflammation signals from stromal cells and the epithelial cells will drive abnormal states to produce a cytokine storm that fuels malignant growth. Inhibitors to RIPK2 may have promising therapeutic potential to uniquely interfere with NFκB-dependent biology and offer an alternative to existing anti-inflammatory therapies.

Acknowledgments

The authors thank all the members of the Baksh laboratory for their helpful discussions.

Authorship Contributions

Conducted experiments: Salla, Aguayo-Ortiz, Ibrahim, Zare, Said, Blankstein, Fong, Manaloor, Pandya, Bhullar, Fiteh, Moore, Baksh.

Participated in research design: Salla, Aguayo-Ortiz, Gibson, Goping, Velázquez-Martínez, Vliagoftis, Brocks, Hubbard, Baksh.

Performed data analysis: Salla, Aguayo-Ortiz, Hwang, Moore, Blankstein, Garcia, Meier, Baksh.

Wrote or contributed to the writing of the manuscript: Salla, Aguayo-Ortiz, Baksh.

References

Bernstein FC, Koetzle TF, Williams GJ, Meyer EF, Jr, Brice MD, Rodgers JR, Kennard O, Shimanouchi T, and Tasumi M (1977) The protein data bank: a computer-based archival file for macromolecular structures. *J Mol Biol* **112**: 535–542.

Borisa AC and Bhatt HG (2017) A comprehensive review on Aurora kinase: small molecule inhibitors and clinical trial studies. *Eur J Med Chem* **140**:1–19.

Branquinho D, Freire P, and Sofia C (2016) NOD2 mutations and colorectal cancer - Where do we stand? *World J Gastrointest Surg* **8**:284–293.

Canning P, Ruan Q, Schwerd T, Hrdinka M, Maki JL, Saleh D, Suebsuwong C, Ray S, Brennan PE, Cuny GD, et al. (2015) Inflammatory signaling by NOD-RIPK2 is inhibited by clinically relevant type II kinase inhibitors. *Chem Biol* **22**:1174–1184.

Downloaded from jpet.aspetjournals.org at ASPET Journals on April 4, 2018

Cao Y, Charisi A, Cheng LC, Jiang T, and Girke T (2008) ChemmineR: a compound mining framework for R. *Bioinformatics* **24**:1733–1734.
Chirieleison SM, Kertesy SB, and Abbott DW (2016) Synthetic biology reveals the uniqueness of the RIP kinase domain. *J Immunol* **196**:4291–4297.
Dai H, Ellis JL, Sinclair DA, and Hubbard BP (2016) Synthesis and assay of SIRT1-activating compounds. *Methods Enzymol* **574**:213–244.
Delaglio F, Grzesiek S, Vuister GW, Zhu G, Pfeifer J, and Bax A (1995) NMRPipe: a multidimensional spectral processing system based on UNIX pipes. *J Biomol NMR* **6**:277–293.
Dieleman LA, Palmen MJ, Akol H, Bloemena E, Peña AS, Meuwissen SG, and Van Rees EP (1998) Chronic experimental colitis induced by dextran sulphate sodium (DSS) is characterized by Th1 and Th2 cytokines. *Clin Exp Immunol* **114**:385–391.
Dyson JK and Rutter MD (2012) Colorectal cancer in inflammatory bowel disease: what is the real magnitude of the risk? *World J Gastroenterol* **18**:3839–3848.
Ermann J, Staton T, Glickman JN, de Waal Malefyt R, and Glimcher LH (2014) Nod/Ripk2 signaling in dendritic cells activates IL-17A-secreting innate lymphoid cells and drives colitis in T-bet-/-.Rag2-/- (TRUC) mice. *Proc Natl Acad Sci USA* **111**: E2559–E2566.
Gonçalves P, Magro F, and Martel F (2015) Metabolic inflammation in inflammatory bowel disease: crosstalk between adipose tissue and bowel. *Inflamm Bowel Dis* **21**: 453–467.
Gordon M, El-Kalla M, Zhao Y, Fiteih Y, Law J, Volodko N, Anwar-Mohamed A, El-Kadi AO, Liu L, Odenbach J, et al. (2013) The tumor suppressor gene, RASSF1A, is essential for protection against inflammation -induced injury [published correction appears in *PLoS One* (2014) 9(1)]. *PLoS One* **8**:e75483.
Haile PA, Votta BJ, Marquis RW, Bury MJ, Mehlmann JF, Singhaus R, Jr, Charnley AK, Lakdawala AS, Convery MA, Lipshutz DB, et al. (2016) The identification and pharmacological characterization of 6-(tert-butylsulfonyl)-N-(5-fluoro-1H-indazol-3-yl)quinolin-4-amine (GSK583), a highly potent and selective inhibitor of RIP2 kinase. *J Med Chem* **59**:4867–4880.
Hayden MS and Ghosh S (2004) Signaling to NF-kappaB. *Genes Dev* **18**:2195–2224.
He X, Da Ros S, Nelson J, Zhu X, Jiang T, Okram B, Jiang S, Michellys PY, Iskandar M, Espinola S, et al. (2017) Identification of potent and selective RIPK2 inhibitors for the treatment of inflammatory diseases. *ACS Med Chem Lett* **8**:1048–1053.
Jun JC, Cominelli F, and Abbott DW (2013) RIP2 activity in inflammatory disease and implications for novel therapeutics. *J Leukoc Biol* **94**:927–932.
Kim S, Thiessen PA, Bolton EE, Chen J, Fu G, Gindulyte A, Han L, He J, He S, Shoemaker BA, et al. (2016) PubChem substance and compound databases. *Nucleic Acids Res* **44** (D1):D1202–D1213.
Kitzenberg D, Colgan SP, and Glover LE (2016) Creatine kinase in ischemic and inflammatory disorders. *Clin Transl Med* **5**:31.
Koes DR and Camacho CJ (2012) Small-molecule inhibitor starting points learned from protein-protein interaction inhibitor structure. *Bioinformatics* **28**:784–791.
Kühn R, Löhler J, Rennick D, Rajewsky K, and Müller W (1993) Interleukin-10-deficient mice develop chronic enterocolitis. *Cell* **75**:263–274.
Kumar RK, Herbert C, and Foster PS (2008) The "classical" ovalbumin challenge model of asthma in mice. *Curr Drug Targets* **9**:485–494.
Lagorce D, Sperandio O, Baell JB, Miteva MA, and Villoutreix BO (2015) FAF-Drugs3: a web server for compound property calculation and chemical library design. *Nucleic Acids Res* **43** (W1):W200–W207.
Lasry A, Zinger A, and Ben-Neriah Y (2016) Inflammatory networks underlying colorectal cancer. *Nat Immunol* **17**:230–240.
Lipinski CA, Lombardo F, Dominy BW, and Feeney PJ (2001) Experimental and computational approaches to estimate solubility and permeability in drug discovery and development settings. *Adv Drug Deliv Rev* **46**:3–26.
Lupfer C, Thomas PG, Anand PK, Vogel P, Milasta S, Martinez J, Huang G, Green M, Kundu M, Chi H, et al. (2013) Receptor interacting protein kinase 2-mediated mitophagy regulates inflammasome activation during virus infection. *Nat Immunol* **14**:480–488.
Lupfer CR, Anand PK, Liu Z, Stokes KL, Vogel P, Lamkanfi M, and Kanneganti TD (2014) Reactive oxygen species regulate caspase-11 expression and activation of the non-canonical NLRP3 inflammasome during enteric pathogen infection. *PLoS Pathog* **10**:e1004410.
Madrid LV and Baldwin AS, Jr (2003) Regulation of NF-kappaB by oncoproteins and tumor suppressor proteins. *Methods Mol Biol* **223**:523–532.
Madsen K, Cornish A, Soper P, McKaigney C, Jijon H, Yachimec C, Doyle J, Jewell L, and De Simone C (2001) Probiotic bacteria enhance murine and human intestinal epithelial barrier function. *Gastroenterology* **121**:580–591.
Moriwaki K, Bertin J, Gough PJ, Orlowski GM, and Chan FK (2015) Differential roles of RIPK1 and RIPK3 in TNF-induced necroptosis and chemotherapeutic agent-induced cell death. *Cell Death Dis* **6**:e1636.
Morris GM, Huey R, Lindstrom W, Sanner MF, Belew RK, Goodsell DS, and Olson AJ (2009) AutoDock4 and AutoDockTools4: automated docking with selective receptor flexibility. *J Comput Chem* **30**:2785–2791.
Murgueitio MS, Rakers C, Frank A, and Wolber G (2017) Balancing inflammation: computational design of small-molecule toll-like receptor modulators. *Trends Pharmacol Sci* **38**:155–168.
Nachbur U, Stafford CA, Bankovacki A, Zhan Y, Lindqvist LM, Fiil BK, Khakham Y, Ko HJ, Sandow JJ, Falk H, et al. (2015) A RIPK2 inhibitor delays NOD signalling events yet prevents inflammatory cytokine production. *Nat Commun* **6**:6442.
Nakashima K, Hirota T, Suzuki Y, Akahoshi M, Shimizu M, Jodo A, Doi S, Fujita K, Ebisawa M, Yoshihara S, et al. (2006) Association of the RIP2 gene with childhood atopic asthma. *Allergol Int* **55**:77–83.
O'Boyle NM, Banck M, James CA, Morley C, Vandermeersch T, and Hutchison GR (2011) Open babel: an open chemical toolbox. *J Cheminform* **3**:33.
Orlowski RZ and Baldwin AS, Jr (2002) NF-kappaB as a therapeutic target in cancer. *Trends Mol Med* **8**:385–389.
Ostojic SM (2017) Mitochondria-targeted nutraceuticals in sports medicine: a new perspective. *Res Sports Med* **25**:91–100.
Owens BM, Steevels TA, Dudek M, Walcott D, Sun MY, Mayer A, Allan P, and Simmons A (2013) CD90(+) stromal cells are non-professional innate immune effectors of the human colonic mucosa. *Front Immunol* **4**:307.
Pettersen EF, Goddard TD, Huang CC, Couch GS, Greenblatt DM, Meng EC, and Ferrin TE (2004) UCSF Chimera–a visualization system for exploratory research and analysis. *J Comput Chem* **25**:1605–1612.
Sterling T and Irwin JJ (2015) ZINC 15--ligand discovery for everyone. *J Chem Inf Model* **55**:2324–2337.
Suman S, Sharma PK, Rai G, Mishra S, Arora D, Gupta P, and Shukla Y (2016) Current perspectives of molecular pathways involved in chronic inflammation-mediated breast cancer. *Biochem Biophys Res Commun* **472**:401–409.
Tang BL (2016) Sirt1 and the mitochondria. *Mol Cells* **39**:87–95.
Tigno-Aranjuez JT, Asara JM, and Abbott DW (2010) Inhibition of RIP2's tyrosine kinase activity limits NOD2-driven cytokine responses. *Genes Dev* **24**:2666–2677.
Tigno-Aranjuez JT, Benderitter P, Rombouts F, Deroose F, Bai X, Mattioli B, Cominelli F, Pizarro TT, Hoflack J, and Abbott DW (2014) In vivo inhibition of RIPK2 kinase alleviates inflammatory disease. *J Biol Chem* **289**:29651–29664.
Trott O and Olson AJ (2010) AutoDock Vina: improving the speed and accuracy of docking with a new scoring function, efficient optimization, and multithreading. *J Comput Chem* **31**:455–461.
Vanden Berghe T, Hassannia B, and Vandenabeele P (2016) An outline of necrosome triggers. *Cell Mol Life Sci* **73**:2137–2152.
Vieira SM, Cunha TM, França RF, Pinto LG, Talbot J, Turato WM, Lemos HP, Lima JB, Verri WA, Jr, Almeida SC, et al. (2012) Joint NOD2/RIPK2 signaling regulates IL-17 axis and contributes to the development of experimental arthritis. *J Immunol* **188**:5116–5122.
Vriend G (1990) WHAT IF: a molecular modeling and drug design program. *J Mol Graph* **8**:52–56, 29.
Williamson KD and Chapman RW (2015) Primary sclerosing cholangitis: a clinical update. *Br Med Bull* **114**:53–64.
Wu S, Kanda T, Nakamoto S, Imazeki F, and Yokosuka O (2012) Knockdown of receptor-interacting serine/threonine protein kinase-2 (RIPK2) affects EMT-associated gene expression in human hepatoma cells. *Anticancer Res* **32**: 3775–3783.

Address correspondence to: Dr. Shairaz Baksh, Division of Hematology/Oncology, Department of Pediatrics, Faculty of Medicine and Dentistry, 3-020E Katz Group Centre for Pharmacy and Health Research, 113 Street 87 Avenue, University of Alberta, Edmonton, AB T6G 2E1, Canada. E-mail: sbaksh@ualberta.ca

Downloaded from jpet.aspetjournals.org at ASPET Journals on April 4, 2018

Identification and Characterization of Novel Receptor Interacting Serine/threonine-Protein Kinase 2 (RIPK2) Inhibitors Using Structural Similarity Analysis

Mohamed Salla, Rodrigo Aguayo-Ortiz, Danmaliki G. Ibrahim, Alaa Zare, Ahmed Said, Jack Moore, Vrajeshkumar Pandya, Robin Manaloor, Sunny Fong, Anna R. Blankstein, Spencer B. Gibson, Laura Ramos Garcia, Pascal Meier, Khushwant Singh Bhullar, Basil P. Hubbard, Yahya Fiteh, Harissios Vliagoftis, Ing Swie Goping, Dion Brocks, Peter Hwang, Carlos A. Velázquez-Martínez and Shairaz Baksh

Departments of Biochemistry (M.S.; D.G.I.; A.S.; J.K. V.P.; I.N.G.; P.H. S.B.), Pediatrics (A.Z.; R. M.; S.F.; S.B.), Pharmacology (K.S.B.; B.P.H), Oncology (S.B.) Medicine (Y.H.; H.V, P.H) and Faculty of Pharmacy and Pharmaceutical Sciences (R.A.O.; D.B.; C.V.M.) University of Alberta 113 Street 87 Avenue, Edmonton, Alberta, Canada. T6G 2E1. Facultad de Química, Departamento de Farmacia, Universidad Nacional Autónoma de México (R.A.O.) Departments of Biochemistry and Medical Genetics and Immunology (A.R.B.; S.B.G.;) University of Manitoba. Breakthrough Breast Cancer Research Center (L.R.G.; P.M.) Chester Beatty Laboratories 237 Fulham Road, London, UK SW3 6JB. Cancer Research Institute of Northern Alberta (S.B.), Edmonton, AB, Canada. T6G 2R7) and Women and Children's Health Research Institute (S.B.) (4-081 Edmonton Clinic Health Academy [ECHA] 11405 87 Avenue NW Edmonton, AB T6G 1C9)

Supplementary Information, Experimental Procedures

Pharmacokenetics. Intraperitoneal injection of 15 µg/kg body weight of RIPK2 inhibitor 1 was carried out on wild type C56BL/6 mice**.** At the indicated times, cardiac puncture was performed and mouse serum obtained. Inhibitor 1 was measured in mouse serum injected using a high performance liquid chromatographic (HPLC) assay. To 0.1 mL of mouse serum in glass tubes was added 0.05 mL each of 1 M NaOH and methanol. This was followed by addition of 3 mL of t-butyl methyl ether, vortex mixing for 30 sec at high speed, and centrifugation at high speed for 3 min. The supernatant was transferred to clean glass tubes and the solvent evaporated *in vacuo*. The residue was reconstituted in 0.15 mL of mobile phase and 0.05 mL injected into the HPLC. The mobile phase was a mixture of [25 mM KH_2PO_4: 3 mM sulfuric acid: 3.6 mM triethylamine]: acetonitrile in the proportion 64:36 v/v. The mobile phase was passed (0.9 mL/min at room temperature) in series through a C18 2 cm×4.0mm, 5m guard column (Supelco, PA, USA) then a Symmetry C18 analytical column, 3.5m, 150mm×4.6mm (Waters, MA, USA). Chromatographic data were collected and compiled by use of EZChrom software.

Detection was by ultraviolet absorption using a Waters 486 detector, with the λ_{max} being set to 261 nm. Standard curves of peak area or height from 25 to1000 ng/mL were highly linear ($r^2 > 0.99$).

Kinase Profiling. All assays are carried out in 97 well plate format as service at DiscoverX using their 97 target KinomeScan Profiling Service. For the 97 KinomeScan profiling assay, competition binding assays were carried as described previously (Karaman et al., 2008). Briefly, kinases were generated either as full length fusions to T7 phage6 or expressed in HEK-293 cells and subsequently tagged with DNA for PCR detection. For the binding assays, biotinylated affinity resins were coupled to streptavidin-coated magnetic beads, blocked with excess biotin and washed with blocking buffer (SeaBlock, Pierce) to remove unbound ligand and to reduce nonspecific binding. Binding reactions were initiated by combining kinase, liganded affinity beads and test compounds in binding buffer. Test compounds were prepared as 100 x stocks in DMSO and rapidly diluted into the aqueous environment. DMSO was added to control assays lacking a test compound. The assay plates containing kinase/ligand and small molecule inhibitor were incubated at 25 °C with shaking for 1 h, washed extensively to remove unbound protein and eluted. The kinase concentration in the eluates was measured by quantitative PCR. Each kinase was tested individually against each compound. *K*ds were determined using eleven serial threefold dilutions.

Kinase Activity Assay for c-Abl. C-Abl kinase assay (Fig. 4D) was carried out by the MRC Protein Phosphorylation and Ubiquitylation Unit at http://www.ppu.mrc.ac.uk/. ABL (5-20mU diluted in 50 mM Tris pH 7.5, 0.1 mM EGTA, 1 mg/ml BSA) is assayed against substrate peptide (EAIYAAPFAKKK) in a final volume of 25.5 µl containing 50mM Tris pH 7.5, 0.1 mM EGTA, 1mM DTT, 300µM substrate peptide, 10 mM magnesium acetate and 0.005 mM [33P-γ-ATP] (50-1000 cpm/pmole) and incubated for 30 min at room temperature. Assays are stopped by addition of 5µl of 0.5 M (3%) orthophosphoric acid and then harvested onto P81 Unifilter plates with a wash buffer of 50 mM orthophosphoric acid. The dried Unifilter plates are then sealed on the addition of MicroScint O and are counted in Packard Topcount NXT scintillation counters.

MTT Growth Assay. Cell proliferation assay was performed to evaluate cell viability after drug treatment. Cells were counted using hemocytometer and seeded in a 96-well plate at 1-2 X 10^4 cells/well and incubated for 24 hours. Different concentrations of RIPK2 inhibitor was added to the cells and incubated for 48h. MTT [3-(4,5-Dimethylthiazol-2-yl)-2,5-Diphenyltetrazolium Bromide] was then added and incubated for 4h. Absorbance was measured at 560 nm using vICToR™ Multilabel Plate Reader from PerkinElmer. For L428, cells were stained with Trypan Blue to determine cell viability after 1 – 6 days incubation with the drugs.

Immunoblot and Immunoprecipitation Analysis. Cells were collected and lysed using RIPA lysis buffer. Samples are denatured in SDS sample buffer and ran on 7.5% gel and blotted onto PVDF membrane. Blotted membranes are blocked with 10% milk for 30min

and then incubated with primary antibodies overnight at 4ºC. Membranes are then washed TBS-T (Tris-buffered saline containing 0.1% Tween 20) and incubated with appropriate secondary antibody (anti-rabbit or anti-mouse IgG) for one hour.

Cell cycle analysis. MCF-7 or HCT116 cells were grown in 6-well plates and treated with the indicated compounds. Post-treatment, cells were trypsinised and resuspended in complete growth medium followed by centrifugation (230xg) and a 1XPBS wash. Cell pellets were gently resuspended in ice-cold 70% ethanol and a single cell suspension was made by gentle vortexing followed by overnight storage at -20°C. Next day, ethanol fixed cells were centrifuged (500xg) and washed twice with 1XPBS at 4°C. Propidium iodide staining of the cells was performed by incubating cell pellets in DNA staining solution (0.1% TritonX-100, 100 µg/ml DNAse free RNAseA, 20 µg/ml propidium iodide in 1XPBS) at 37°C for 30min followed by filtration through a nylon mesh (50 µM exclusion limit) to remove cell clumps. Flow cytometric analysis of was performed on a BD Accuri cell analyser).

RIPK1 activity. HT-29, L929 and HaCaT cells were seeded in a 96-well plate and then treated with the indicated amounts of RIPK2 inhibitors. After 24 hours, the media was removed and replaced with fresh media containing 20 µM z-VAD-fmk (Z), 100 nM Smac Mimetic-164 (S) and 10 ng/mL TNFα (T) in the presence or absence of 100 nM Ripk1 inhibitor or 1 uM necrosulfanamide (NSA) or the indicated amounts of RIPK2 inhibitors for 24 hours (HaCaT and HT-29) or 8 h (L929). After the indicated time, the cells were double stained with hoechst and propidium iodide for 30 minutes at 37 degrees and then cell death was measured using the Celigo cell cytometer.

Ferroptosis Analysis. A549 and U87 cells plated in 12 well dishes were pretreated with the inhibitors for one hour before the cells were treated with Erastin (a compound known to induce ferroptosis). After 48 hours, cells were harvested, re-suspended in PBS and stained with 0.04% trypan blue for 5-10 minutes at room temperature. Cell death was quantified by flow cytometry using the FACSCalibur flow cytometer and CellQuest software. Ferrostatin-1 (Fer-1) and Deferoxamine (DFO) were used as positive controls for the inhibition of ferroptosis.

Assay of SIRT1 activity. The BIOMOL (Enzo Life Sciences) assay was performed as previously described (Hubbard et al., 2013). 2µg of recombinant SIRT1 was used for each reaction, and the β-NAD and FdL-p53 peptide concentrations used were 200 µM and 20 µM, respectively. 0.5 µL of vehicle or test compound was added to each 50 µL reaction. Fluorescence values corresponding to SIRT1 activity were calculated by subtracting parallel reactions in the absence of β-NAD from those in the presence of β-NAD ($F_{corrected} = F_{+NAD} - F_{-NAD}$). Fold activation was calculated by dividing fluorescence values in the presence of drug by those in the presence of DMSO only.

Supplementary Information, Tables and Figures

Supplemental Table 1. Related to Table 1. Pharmacophore (Pharm) and similarity (Sim) compound ranking, PCFP similarity, chemical structure and SMILES of molecules retrieved from the pharmacophore and similarity-based virtual screenings. The compounds were also filtered for PAINS and aggregators (http://zinc15.docking.org/patterns/home/).

Supplemental Table 2. Related to Figure 3. Kinome inhibition in the presence of 100 nM RIPK2 Inhibitor 1or 2. Kinase activity assays of 97 kinases were carried using peptides or defined substrate as carried out by a "Kinome Scan" analysis by the DiscoverX (https://www.discoverx.com/services/drug-discovery-development-services/kinase-profiling/kinomescan/).

Supplemental Figure 1 (A) The ^{1}H-NMRchemical shift assignment of RIPK1 inhibitor 1: 10.32 (s, 1 H), 10.09 (s, 1 H), 8.13 (t, J = 2 Hz, 1H), 8.02 (m, 3H), 7.88 (dt, J = 8 Hz, 2 Hz, 1H) 7.80 (dd, J = 8 Hz, 2Hz, 1H), 7.60-7.64 (m, 1H) 7.52-7.57 (m, 2H) 7.44-7.48 (m, 2H) 7.42 (dt, J = 8 Hz, 2 Hz, 1H) 7.26 (d, J = 2 Hz, 1H) 6.94 (d, J = 2 Hz, 1H) 3.78 (s, 3H) 2.32 (s, 3H) ppm. (B) Analysis of through-space connectivities suggested that RIPK2 inhibitor 1 has two major rotomeric forms in d_6-DMSO. The second rotomer is slightly more favored, perhaps due to the formation of an intramolecular hydrogen bond.

Supplemental Figure 2. (A) The ^{1}H-NMR chemical shift assignment of RIPK1 inhibitor 2: 9.6 (s, 1 H), 8.31 (s, 1 H), 8.00 (dd, J = 9 Hz, 2Hz, 1H), 7.86-7.93 (m, 3H), 7.45-7.52 (m, 2H), 7.37 (d, J = 9 Hz, 2H), 7.09 (d, J = 9 Hz, 2H), 6.9 (s, 1H), 4.32 (br, 1H), 4.10 (br, J = 12 Hz, 5 Hz, 2H) 3.8 (s, 3H), 3.02-3.14 (br, 2H), 2.85-2.92 (br, 2H), 2.78 (sep, J = 7Hz, 1H), 1.9-1.97 (br, 1H), 1.80-1.63 (br, 2H), 1.44-1.54 (br, 2H), 1.40-1.29 (br, 2H), 1.20-1.26 (br, 1H), 1.15 (d, J = 7 Hz, 6H) ppm. Top, enlarged aromatic region; Bottom, full 1D. Note that ^{1}H signals attached to C17-C25 are broadened by conformational exchange, indicating conformational transitions within the fused piperidine ring structure. (B) Two-dimensional ^{1}H-^{1}H ROESY spectrum of [(2R,4S,5R)-5-[1-methyl-3-(naphthalen-2-yl)-1H-pyrazol-5-yl]-1-azabicyclo[2.2.2]octan-2-yl]methyl N-[4-(propan-2-yl)phenyl]carbamate showing through-bond and through-space connections between hydrogen atoms. Boxes (blue) indicate cross peak signals due to 3-bond and 4-bond J-coupling. Signals due to 4-bond J-coupling are less intense. Orange boxes denote through-space ROE connectivities.

Supplemental Figure 3. Related to Figure 2. Mass spectrometry confirmation of mass for RIPK2 Inhibitor 2. (A) Direct-infusion measurements were carried out on an LTQ Orbitrap XL (Thermo Scientific) mass spectrometer using the Ion Max ESI source. Mass confirmation was obtained as indicated. (B) NFκB gene reporter assay of inhibition of NFκB activity with RIPK2 inhibitor 1 (concentration as indicated and several stimuli presented). P values for TNFα treatment was < 0.4; IL-1β was < 0.0007 and IFN-γ was

< 0.07 (for inhibitor 1 treated vs non-treated). (C) RIPK2 inhibitor 1 effect on the activation of hypoxia response element (HRE) activation following 1% H_2O_2 addition overnight. P value for 1% H_2O_2 (treated with inhibitor 1 vs no drug) was < 0.02 (n = 3).

Supplemental Figure 4. Related to Figure 5. Effect of RIPK2 inhibitors on NFκB, cell growth and cell cycle control. (A) EMSA was carried out using the NFκB binding site on the IL-6 promoter. HCT116 cells were pretreated with the indicated RIPK2 inhibitors for 2 days, followed by stimulation with MDP and nuclear/cytoplasmic extraction. Four μg of nuclear extract was incubated with the IL-6 probe in an NFκB DNA binding assay. (B) RIPK2 Inhibitor 1 can modulate the growth of several breast cancer cells. MTT assay was carried out with the 100 nM of RIPK2 inhibitors in the indicated breast cancer cell lines with HCT1143 and MDA-MB31 as triple negative breast cancer cells and JMT-1 is a Her2 overexpressing cell line. For all experiments, n = 4 - 10. P value -/+ RIPK2 inhibitor 1 for JMT-1 was 0.0001, for HCT1143 was 0.0007 and for MDA-MB231 was 0.05. (C) Growth inhibition MTT curves for HCT116 (A) and BT-549 (B, breast cancer cells) were examined in the presence of RIPK2 inhibitor 1 at the concentrations indicated and approximate IC_{50} concentrations determined an indicated on top right portion of the graph.

Supplemental Figure 5. RIPK2 inhibitor 1 does not affect the cell cycle fraction distribution at 100 nM. HCT-116 colon (A) or MCF-7 breast (B) cancer cells were treated with Vehicle or the indicated inhibitors (5 μM) for 36 hours. After an overnight ethanol fixation, cells were PI stained. 15000 cells were analyzed on BD Accuri flow cytometer. Different cell cycle phases were quantitated for 3 independent experiments and plotted as percentage of mean ± SD (far right A and B). No major difference was observed between treatments. The data for 5 μM of the drug is presented but similar results were observed at 100 nM RIPK2 inhibitor 1 drug treated cells.

Supplemental Figure 6. Related to Figure 3, 4 and 5. RIPK2 inhibitors do not inhibit RIP1 or RIP3 Function. (A) Ferroptosis was measured in A549 lung cancer cells following treatment with Erastin. After 48 hours, cells were harvested, re-suspended in PBS and stained with 0.04% trypan blue for 5-10 minutes at room temperature. Cell death was quantified by flow cytometry using the FACSCalibur flow cytometer and CellQuest software. P value for Erastin vs. DMSO was < 0.0001; No significant differences were observed for Erastin vs. Erastin + inhibitor (1 or 2) (N=6). Similar results were obtained in the U87 cells. (B) RIPK1 activity was measured in HT-29 cells by activation of cell death using 20 μM z-VAD-fmk (Z), 100 nM Smac Mimetic-164 (S) and 10 ng/mL TNFα (T) combination in the presence or absence of 100 nM Ripk1 inhibitor or 1 μM necrosulfanamide (NSA) or the indicated amounts of RIPK2 inhibitors for 24 hours. After the indicated time, the cells were double stained with hoechst and propidium iodide for 30 minutes at 37 ^{o}C and then cell death was measured using the Celigo cell cytometer. The effect of the RIPK2 inhibitors on RIPK2-directed cell death in L929 and HaCaT cells showed similar results. P value for ZST vs DMSO was < 0.0001. No significant differences

were observed for ZST vs. ZST + inhibitor (1 or 2). (C) Characterization of Sirtuin activity using the BIOMOL (Enzo Life Sciences) assay to monitor NAD activity. (D) Preliminary pharmacokenetics in mouse sera revealed a half-life of 1.89 hour and possible rapid metabolism of RIPK2 inhibitor 1 following 15 μg/g intraperitoneal injection. Upper panel, Chromatograms from untreated mouse serum (bottom trace) and from a mouse serum sample containing 500 ng/mL of inhibitor 1 (upper trace). The inhibitor eluted at 3.7 min. Lower panel, mean ± SD serum concentration vs. time measures of Inhibitor 1 in sera from mice.

Supplemental Figure 7. Related to Table 2 and Figure 6. Mice were exposed to 7 days of 3% DSS to induce inflammation injury and 7 days with water to promote recovery. RIPK2 inhibitors were intraperitoneal (IP) injected on day 5, 7 and 9. Serum was harvested 11 days after last IP injection and blood chemistry was carried out at the Prairie Diagnostics for numerous factors. The ones shown have some significant changes. For alkaline phosphatase, Two-way Anova reveals P value < 0.0001 for all measured marker.

Salla et al., Supplemental Table 1

Pharm Rank	PCFP similarity	ID	Chemical structure and SMILES	PAINS or Aggregators
1	0.781	MolPort-016-359-762	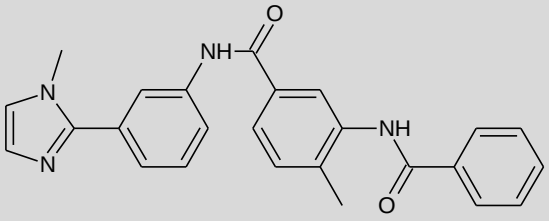 Cc1ccc(cc1NC(=O)c1ccccc1)C(=O)Nc1cccc(c1)-c1nccn1C	NO
2	0.574	MolPort-015-752-252	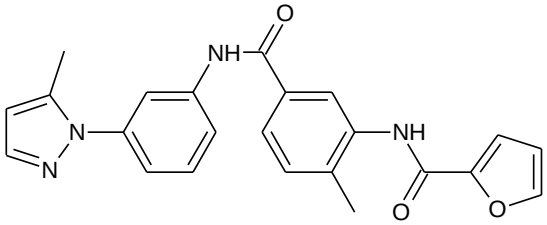 Cc1ccnn1-c1cccc(NC(=O)c2ccc(C)c(NC(=O)c3ccco3)c2)c1	NO
3	0.636	MolPort-015-604-588	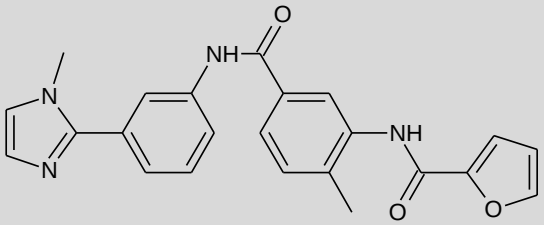 Cc1ccc(cc1NC(=O)c1ccco1)C(=O)Nc1cccc(c1)-c1nccn1C	NO
4	0.630	MolPort-016-412-727	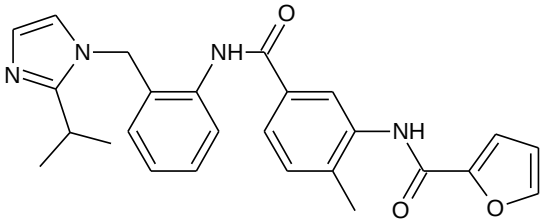 CC(C)c1nccn1Cc1cccc(NC(=O)c2ccc(C)c(NC(=O)c3ccco3)c2)c1	NO
5	< 0.500	ZINC02739307	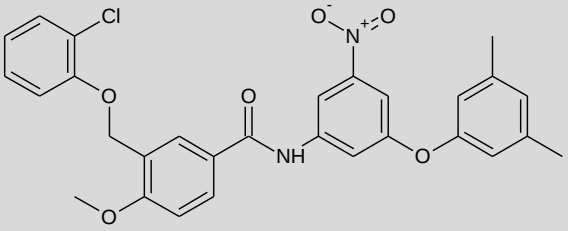 Cc1cc(cc(c1)Oc2cc(cc(c2)[N+](=O)[O-])NC(=O)c3ccc(c(c3)COc4ccccc4Cl)OC)C	NO

Salla et al., Supplemental Table 1 (continued)

Sim Rank	PCFP similarity	PC ID	Chemical structure and SMILES	PAINS or Aggregators
64	0.981	58945685	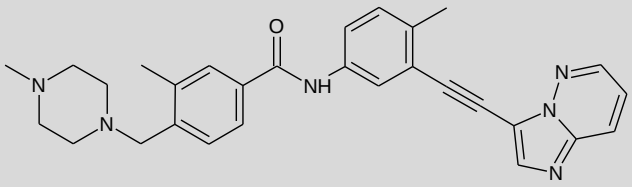 O=C(Nc1cc(c(cc1)C)C#Cc1n2ncccc2nc1)c1cc(c(CN2CCN(CC2)C)cc1)C	NO
65	0.981	58945682	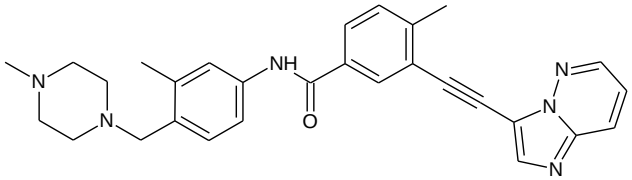 O=C(Nc1cc(c(CN2CCN(CC2)C)cc1)C)c1cc(c(cc1)C)C#Cc1n2ncccc2nc1	NO
95	0.962	24826801	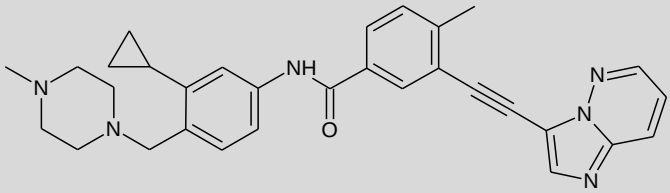 O=C(Nc1cc(C2CC2)c(CN2CCN(CC2)C)cc1)c1cc(c(cc1)C)C#Cc1n2ncccc2nc1	NO
136	0.949	57410628	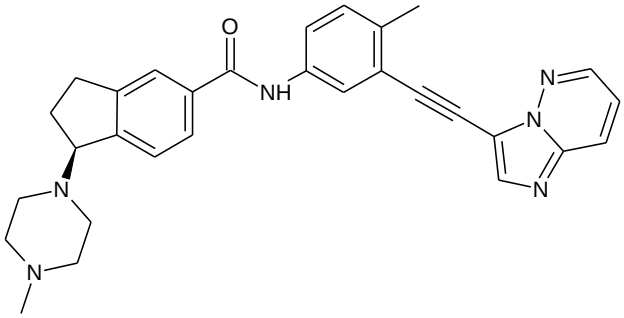 O=C(Nc1cc(c(cc1)C)C#Cc1n2ncccc2nc1)c1cc2c([C@@H](N3CCN(CC3)C)CC2)cc1	NO
137	0.949	57405602	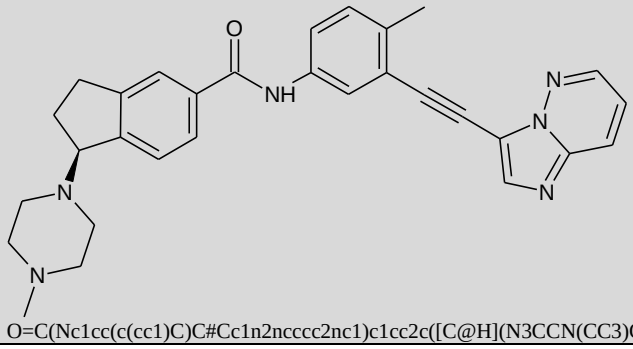 O=C(Nc1cc(c(cc1)C)C#Cc1n2ncccc2nc1)c1cc2c([C@H](N3CCN(CC3)C)CC2)cc1	NO

Salla et al., Supplemental Table 1 (continued)

Sim Rank	PCFP similarity	PC ID	Chemical structure and SMILES	PAINS or Aggregators
168	0.944	68349611	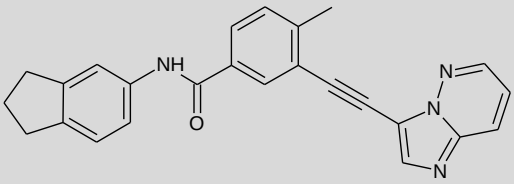 O=C(Nc1cc2CCCc2cc1)c1cc(c(cc1)C)C#Cc1n2ncccc2nc1	NO
619	0.907	58945669	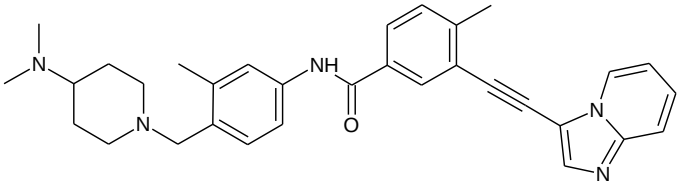 O=C(Nc1cc(c(CN2CCC(N(C)C)CC2)cc1)C)c1cc(c(cc1)C)C#Cc1n2c(nc1)cccc2	NO
724	0.903	58945635	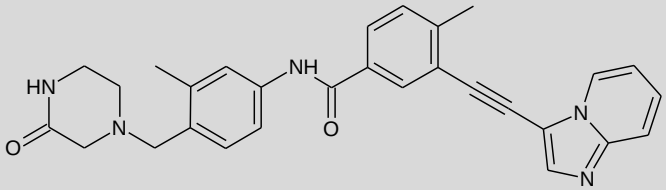 O=C1NCCN(Cc2c(cc(NC(=O)c3cc(c(cc3)C)C#Cc3n4c(nc3)cccc4)cc2)C)C1	NO
8,631,453	0.615	44716361	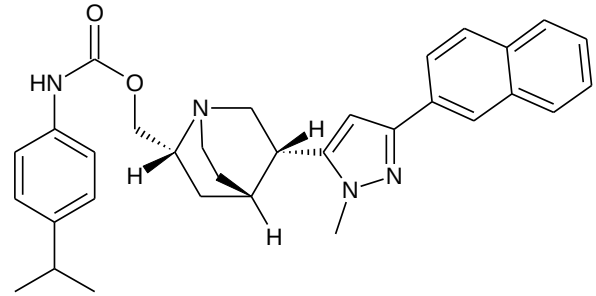 O(C[C@@H]1N2C[C@@H]([C@H](C1)CC2)c1n(nc(c1)c1cc2c(cc1)cccc2)C)C(=O)Nc1ccc(cc1)C(C)C	NO
9,247,462	0.610	40780119	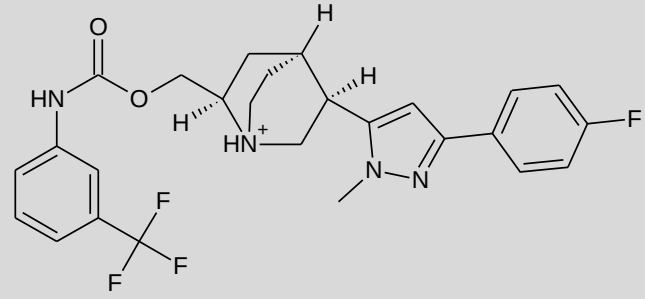 Fc1ccc(c2nn(c([C@@H]3[C@@H]4C[C@@H]([NH+](C3)CC4)COC(=O)Nc3cc(ccc3)C(F)(F)F)c2)C)cc1	NO

Salla et al, Supplemental Table 2

Kinase Species	Entrez Gene Symbol	RIPK2 Inhibitor 1	RIPK2 Inhibitor 2
		% Activity Remaining	% Activity Remaining
ABL1(E255K)-phosphorylated	ABL1	73	93
ABL1(T315I)-phosphorylated	ABL1	96	90
ABL1-nonphosphorylated	ABL1	95	89
ABL1-phosphorylated	ABL1	91	94
ACVR1B	ACVR1B	97	99
ADCK3	CABC1	100	100
AKT1	AKT1	98	97
AKT2	AKT2	86	88
ALK	ALK	90	100
AURKA	AURKA	93	93
AURKB	AURKB	78	97
AXL	AXL	100	97
BMPR2	BMPR2	87	100
BRAF	BRAF	100	96
BRAF(V600E)	BRAF	100	99
BTK	BTK	99	94
CDK11	CDK19	100	93
CDK2	CDK2	100	96
CDK3	CDK3	97	100
CDK7	CDK7	100	100
CDK9	CDK9	99	100
CHEK1	CHEK1	93	88
CSF1R	CSF1R	100	89
CSNK1D	CSNK1D	100	92
CSNK1G2	CSNK1G2	82	73
DCAMKL1	DCLK1	78	100

Salla et al, Supplemental Table 2 (Continued)

Kinase Species	Entrez Gene Symbol	RIPK2 Inhibitor 1	RIPK2 Inhibitor 2
		% Activity Remaining	% Activity Remaining
DYRK1B	DYRK1B	95	94
EGFR	EGFR	93	95
EGFR(L858R)	EGFR	100	81
EPHA2	EPHA2	100	94
ERBB2	ERBB2	72	95
ERBB4	ERBB4	100	100
ERK1	MAPK3	97	91
FAK	PTK2	100	94
FGFR2	FGFR2	93	72
FGFR3	FGFR3	100	85
FLT3	FLT3	89	100
GSK3B	GSK3B	89	73
IGF1R	IGF1R	97	89
IKK-alpha	CHUK	100	100
IKK-beta	IKBKB	100	100
INSR	INSR	100	93
JAK2(JH1domain-catalytic)	JAK2	93	100
JAK3(JH1domain-catalytic)	JAK3	100	100
JNK1	MAPK8	89	73
JNK2	MAPK9	91	93
JNK3	MAPK10	83	81
KIT	KIT	82	100
KIT(D816V)	KIT	100	94
KIT(V559D,T670I)	KIT	100	98
LKB1	STK11	89	95
MAP3K4	MAP3K4	93	94
MAPKAPK2	MAPKAPK2	99	87
MARK3	MARK3	100	100

Salla et al, Supplemental Table 2 (Continued)

Kinase Species	Entrez Gene Symbol	RIPK2 Inhibitor 1	RIPK2 Inhibitor 2
		% Activity Remaining	% Activity Remaining
MEK1	MAP2K1	89	98
MEK2	MAP2K2	83	89
MET	MET	100	69
MKNK1	MKNK1	86	100
MKNK2	MKNK2	100	94
MLK1	MAP3K9	81	82
p38-alpha	MAPK14	100	100
p38-beta	MAPK11	100	97
PAK1	PAK1	98	95
PAK2	PAK2	94	100
PAK4	PAK4	99	100
PCTK1	CDK16	87	90
PDGFRA	PDGFRA	86	88
PDGFRB	PDGFRB	89	100
PDPK1	PDPK1	100	98
PIK3C2B	PIK3C2B	95	100
PIK3CA	PIK3CA	100	100
PIK3CG	PIK3CG	100	100
PIM1	PIM1	100	94
PIM2	PIM2	98	99
PIM3	PIM3	94	100
PKAC-alpha	PRKACA	95	99
PLK1	PLK1	100	100
PLK3	PLK3	82	94
PLK4	PLK4	96	100
PRKCE	PRKCE	100	100
RAF1	RAF1	95	100

Salla et al, Supplemental Table 2 (Continued)

Kinase Species	Entrez Gene Symbol	RIPK2 Inhibitor 1	RIPK2 Inhibitor 2
		% Activity Remaining	% Activity Remaining
RET	RET	100	93
RIOK2	RIOK2	90	93
ROCK2	ROCK2	96	100
RSK2(Kin.Dom.1-N-terminal)	RPS6KA3	99	100
SNARK	NUAK2	100	62
SRC	SRC	98	100
SRPK3	SRPK3	86	78
TGFBR1	TGFBR1	100	96
TIE2	TEK	97	96
TRKA	NTRK1	86	90
TSSK1B	TSSK1B	95	100
TYK2(JH1domain-catalytic)	TYK2	94	100
ULK2	ULK2	84	100
VEGFR2	KDR	96	83
YANK3	STK32C	94	84
ZAP70	ZAP70	100	85

A

RIPK2 Inhibitor 1 - Chemical Structure and Chemical Shift Assignment

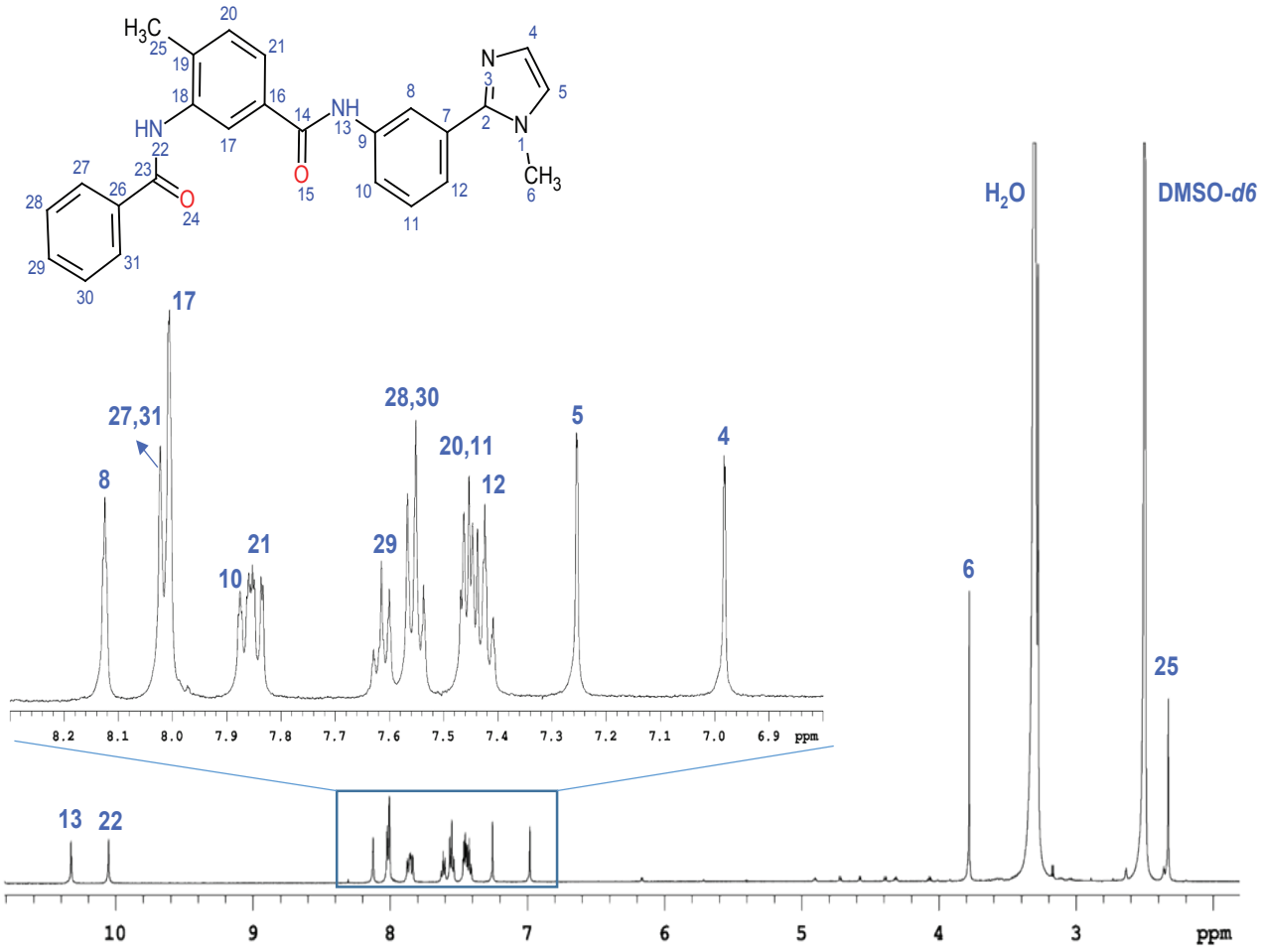

B

RIPK2 Inhibitor 1 Rotomers in Solution

(i)

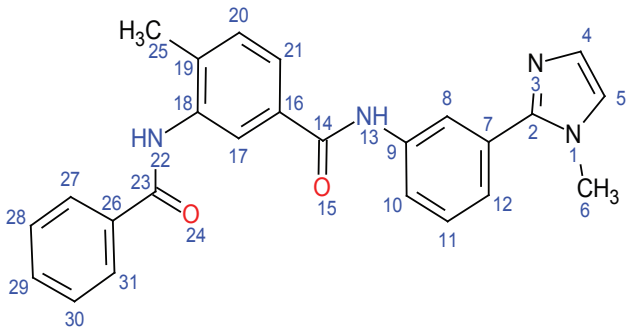

(ii)

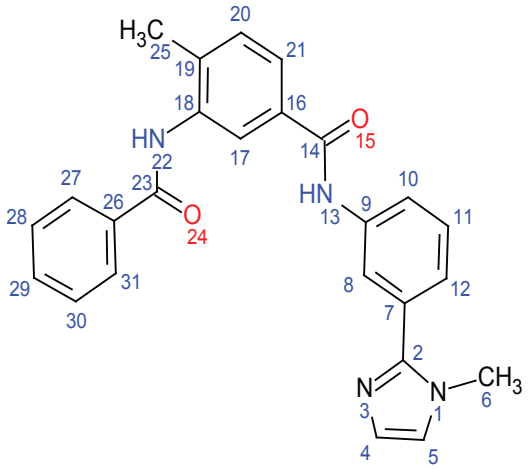

A

RIPK2 Inhibitor 2 - Chemical Structure and Chemical Shift Assignment

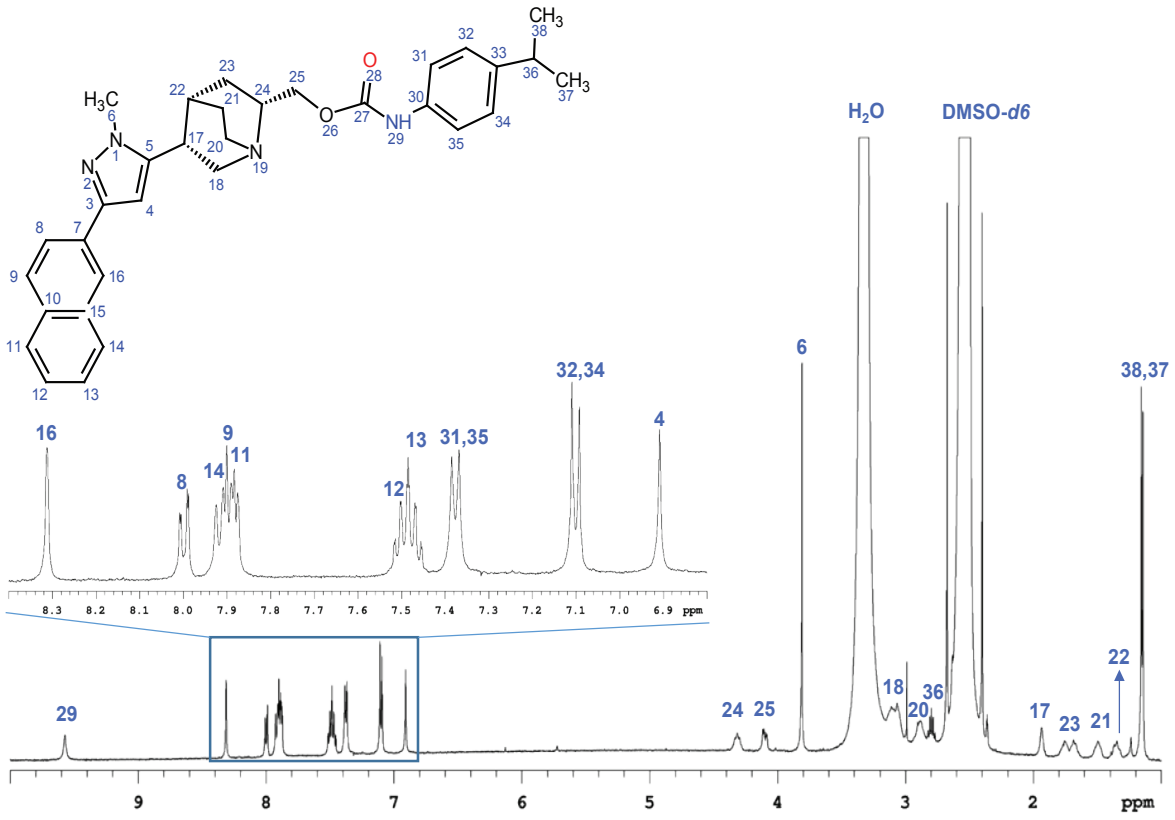

B

RIPK2 Inhibitor 2 - Two Dimensional 1H-1H ROESY Spectrum

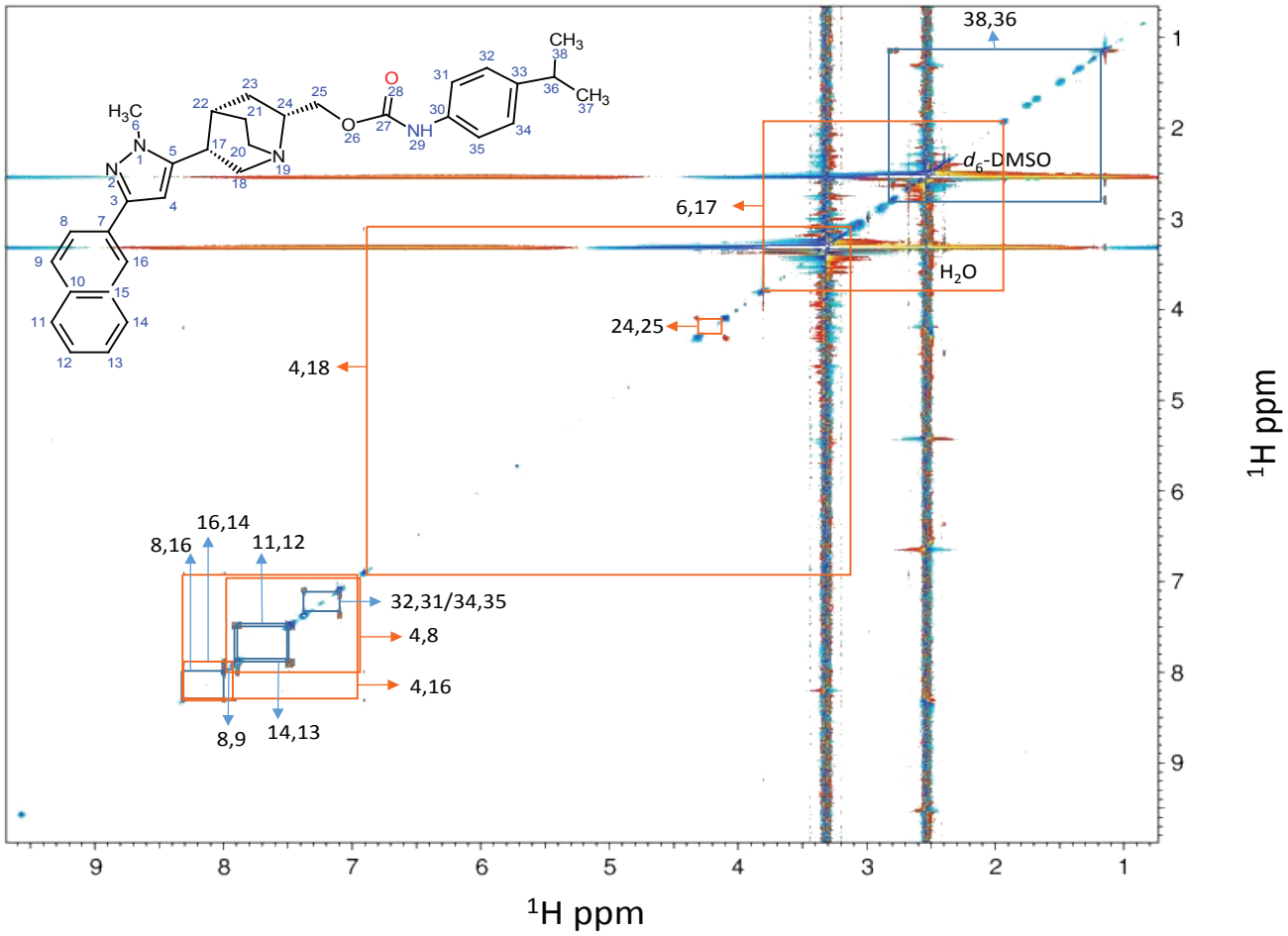

Salla et al, Supplemental Fig 2

A

Mass Spectrometry Confirmation of RIPK2 Inhibitor 2 Formula Weight

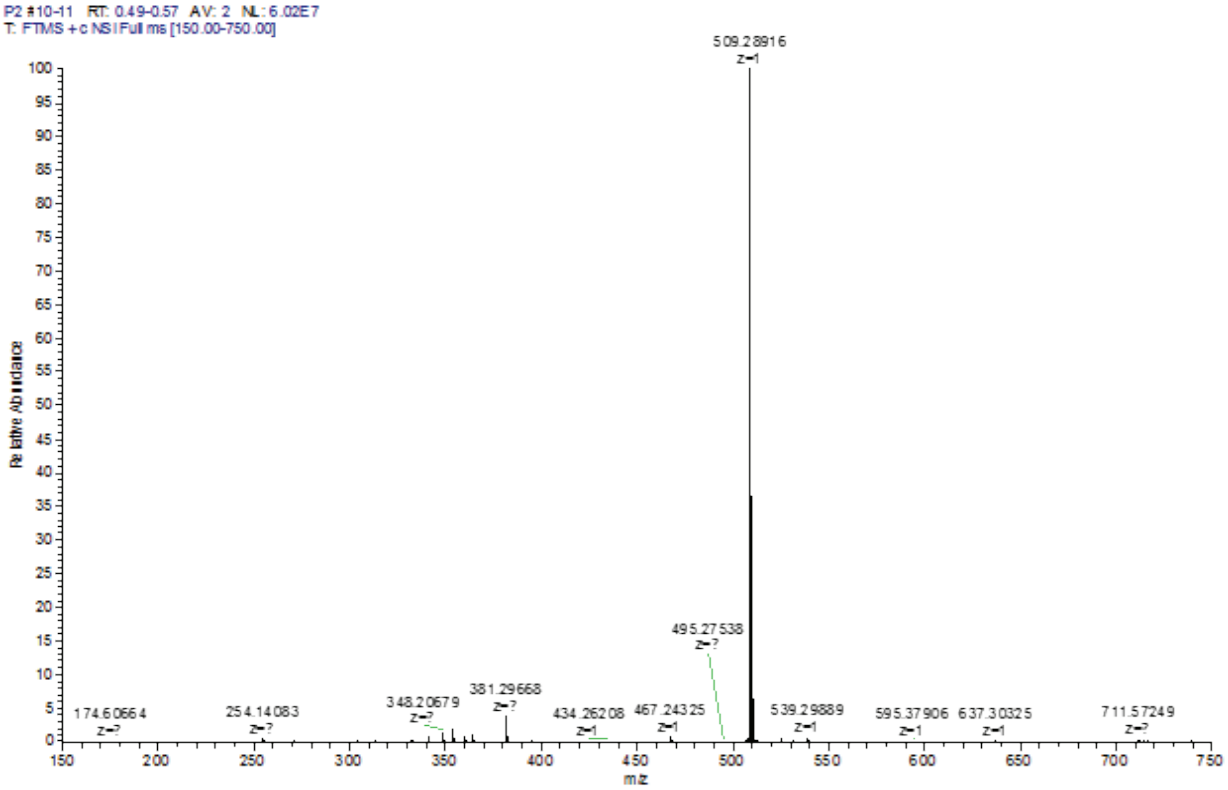

B

Gene Reporter Analysis of RIPK2 Inhibitor 1 inhibition of NFκB Activity

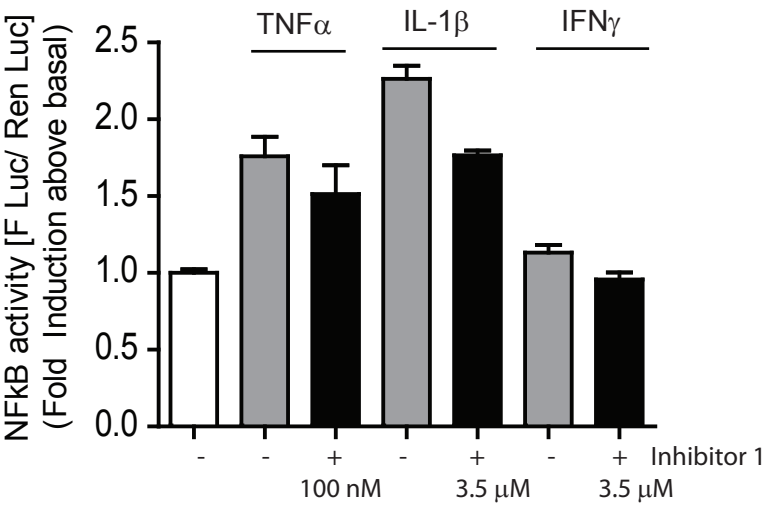

C

Gene Reporter Analysis of RIPK2 Inhibitor 1 inhibition of HRE Activity

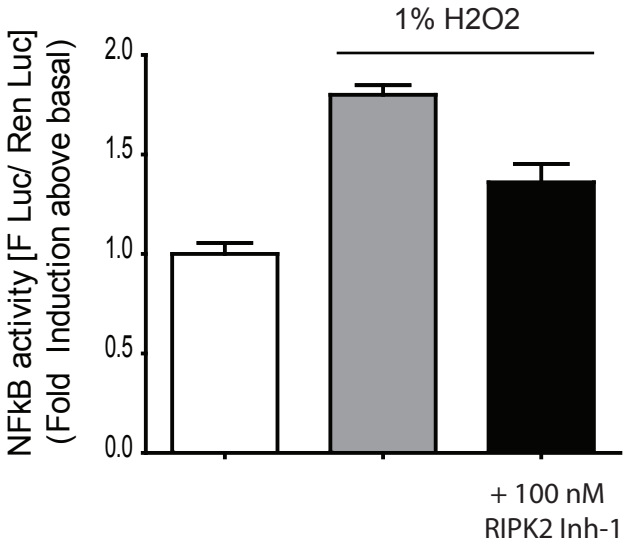

Salla et al, Supplemental Fig. 3

A

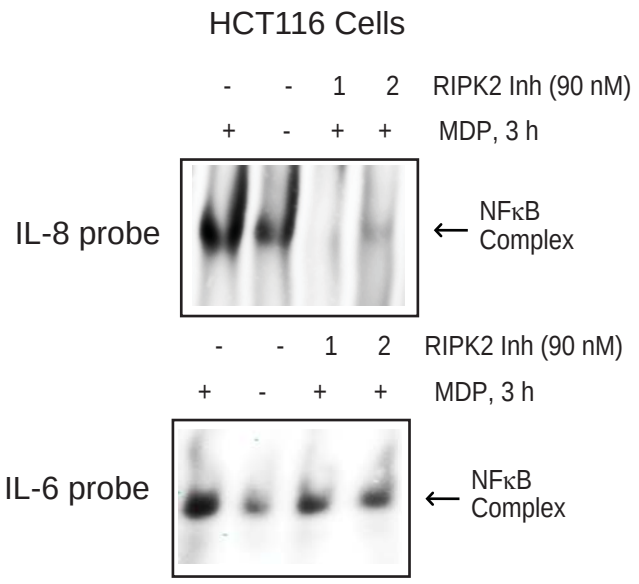
HCT116 Cells
- - 1 2 RIPK2 Inh (90 nM)
+ - + + MDP, 3 h
IL-8 probe
NFκB Complex
- - 1 2 RIPK2 Inh (90 nM)
+ - + + MDP, 3 h
IL-6 probe
NFκB Complex

B

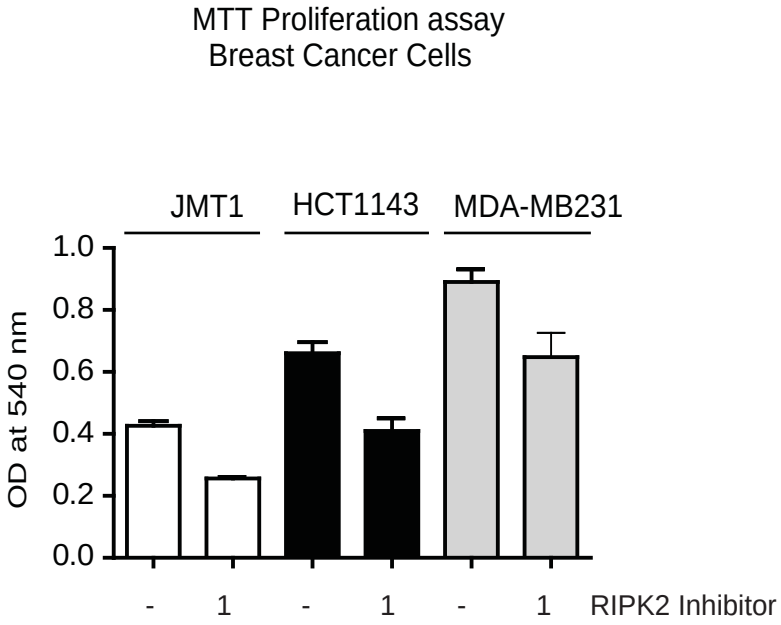
MTT Proliferation assay
Breast Cancer Cells
JMT1
HCT1143
MDA-MB231
OD at 540 nm
1.0
0.8
0.6
0.4
0.2
0.0
- 1 - 1 - 1 RIPK2 Inhibitor

C

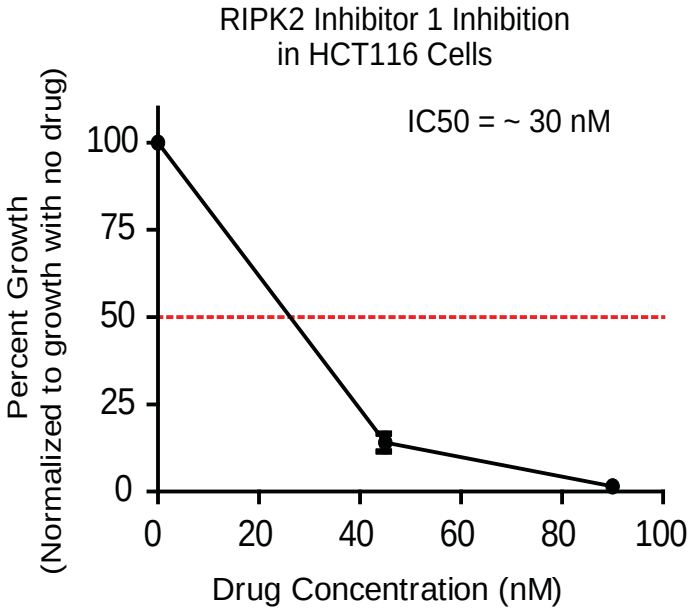
RIPK2 Inhibitor 1 Inhibition
in HCT116 Cells
IC50 = ~ 30 nM
Percent Growth
(Normalized to growth with no drug)
100
75
50
25
0
0 20 40 60 80 100
Drug Concentration (nM)

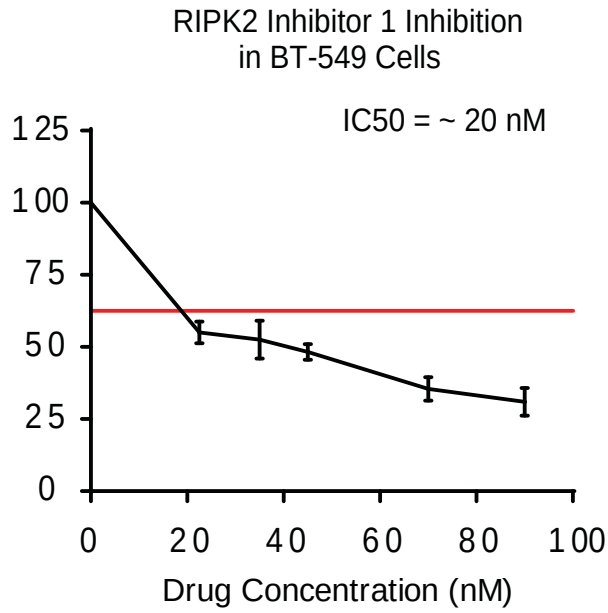
RIPK2 Inhibitor 1 Inhibition
in BT-549 Cells
IC50 = ~ 20 nM
125
100
75
50
25
0
0 20 40 60 80 100
Drug Concentration (nM)

A

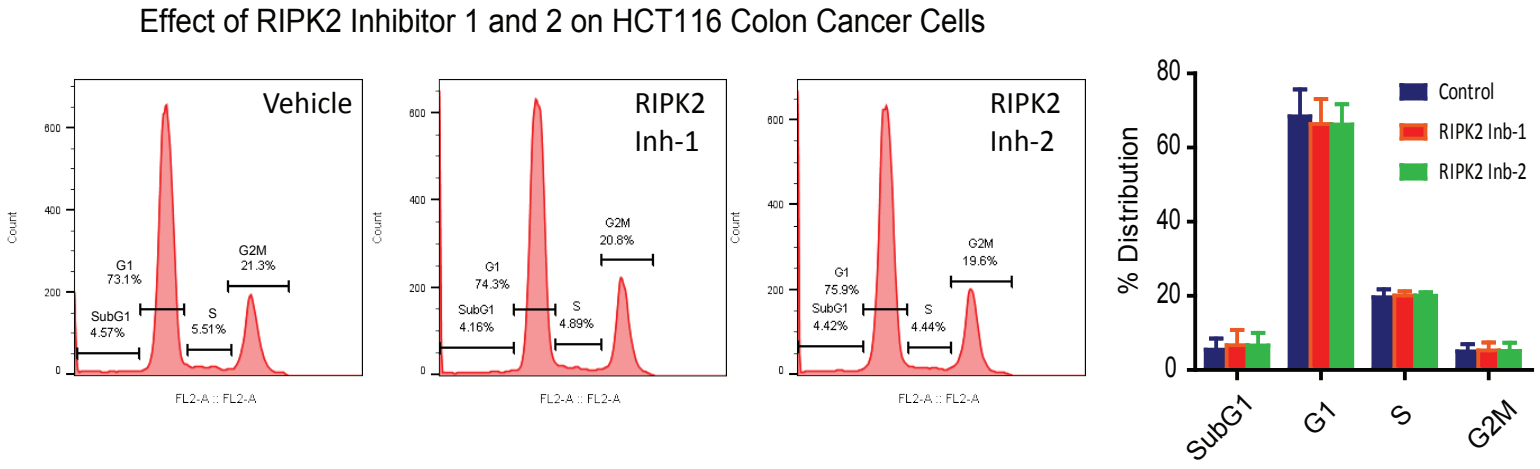
Effect of RIPK2 Inhibitor 1 and 2 on HCT116 Colon Cancer Cells
Vehicle
G1 73.1%
SubG1 4.57%
S 5.51%
G2M 21.3%
RIPK2 Inh-1
G1 74.3%
SubG1 4.16%
S 4.89%
G2M 20.8%
RIPK2 Inh-2
G1 75.9%
SubG1 4.42%
S 4.44%
G2M 19.6%
Count
FL2-A :: FL2-A
% Distribution
Control
RIPK2 Inb-1
RIPK2 Inb-2
SubG1
G1
S
G2M

B

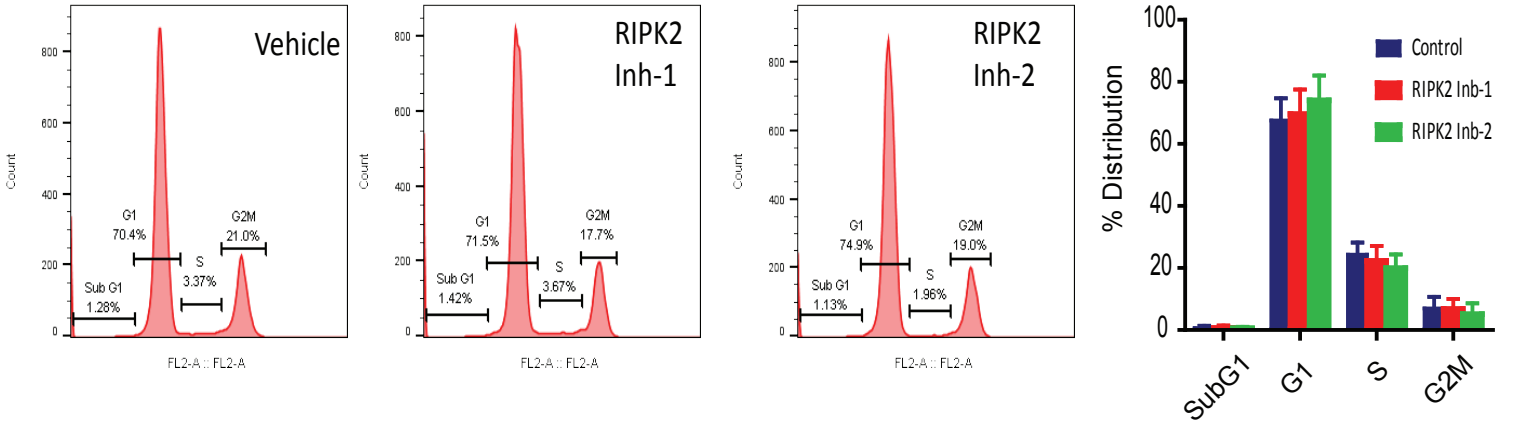
Effect of RIPK2 Inhibitor 1 and 2 on MCF-7 Breast Cancer Cells
Vehicle
G1 70.4%
Sub G1 1.28%
S 3.37%
G2M 21.0%
RIPK2 Inh-1
G1 71.5%
Sub G1 1.42%
S 3.67%
G2M 17.7%
RIPK2 Inh-2
G1 74.9%
Sub G1 1.13%
S 1.96%
G2M 19.0%
Count
FL2-A :: FL2-A
% Distribution
Control
RIPK2 Inb-1
RIPK2 Inb-2
SubG1
G1
S
G2M

A

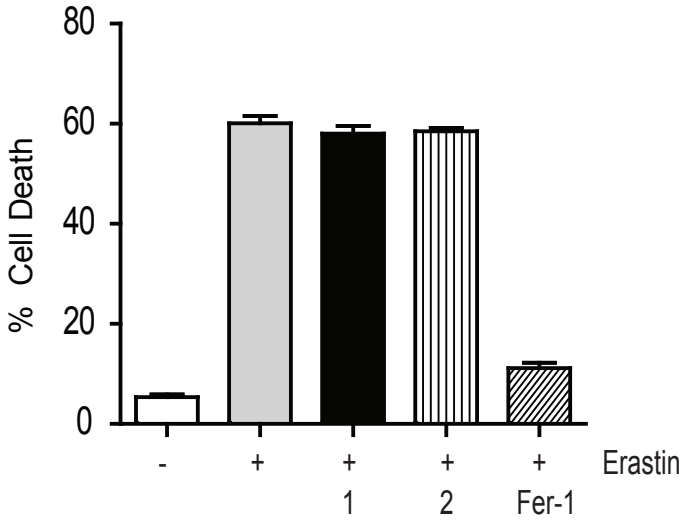

B

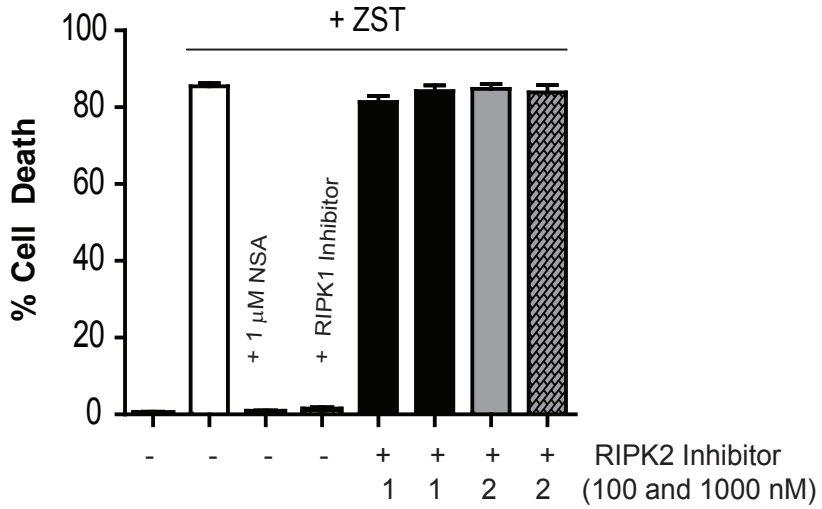

C

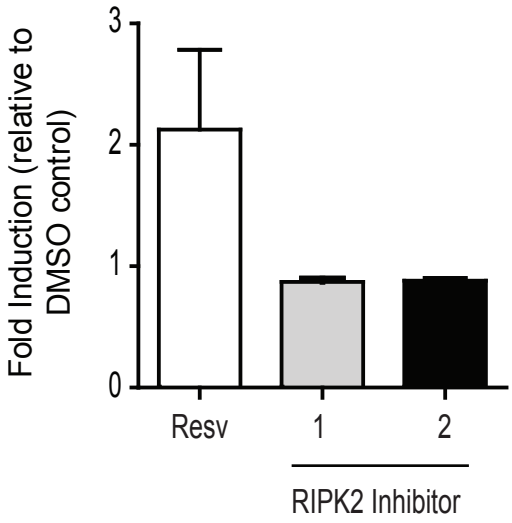

D

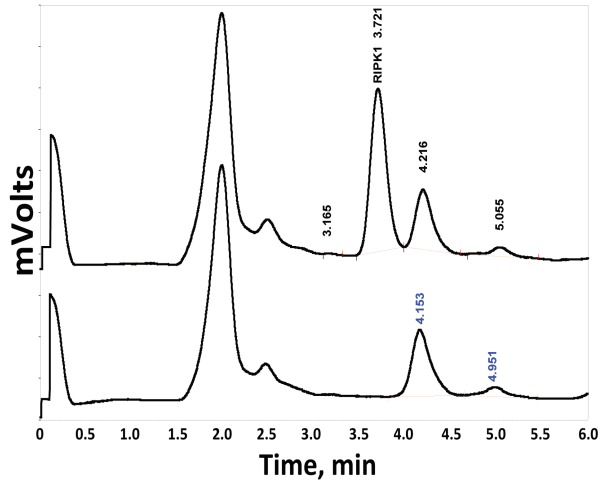

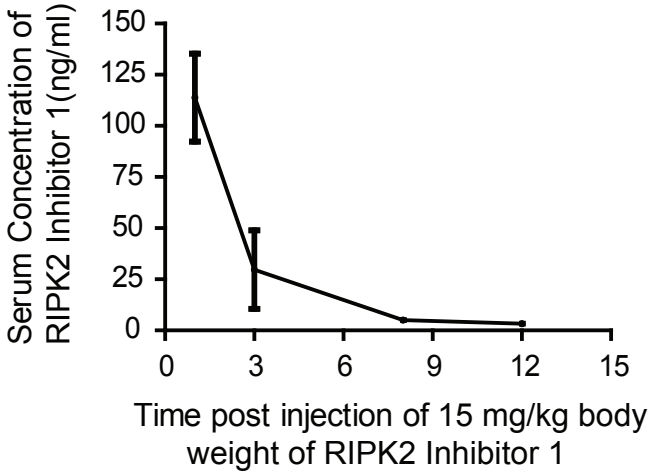

Salla et al, Supplemental Fig.6

RIPK2 inhibitors are well tolerated in vivo
(selected Markers of Tissue Damage shown below)

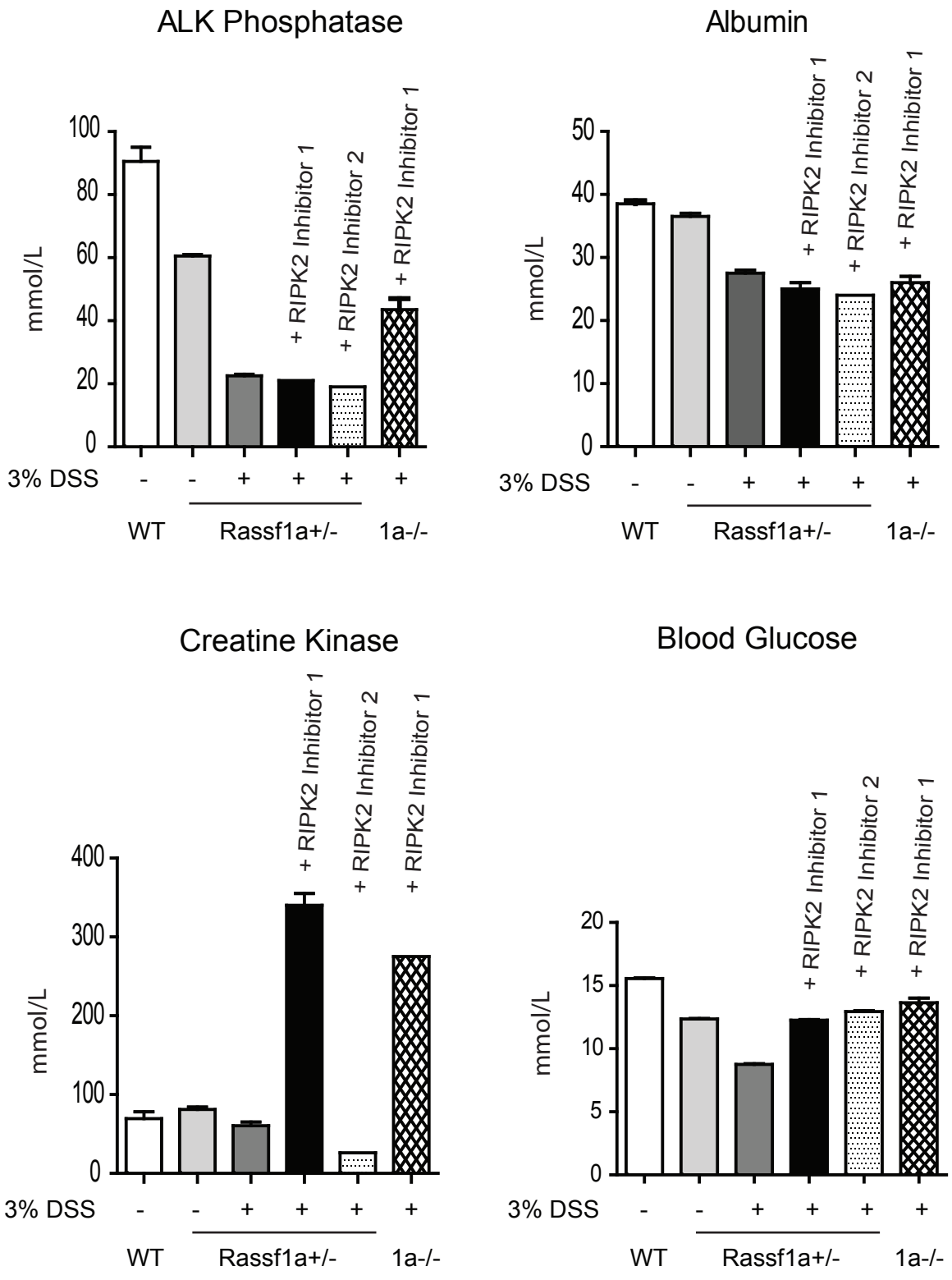

Salla et al, Supplemental Fig.7